

Fe sources and transport from the Antarctic Peninsula shelf to the southern Scotia Sea

Mingshun Jiang^{1*}, Christopher I. Measures², Katherine A Barbeau³, Matthew A. Charette⁴, Sarah
T. Gille³, Mariko Hatta², Mati Kahru³, B. Gregory Mitchell³, Alberto C. Naveira Garabato⁵,
Christian Reiss⁶, Karen Selph², and Meng Zhou⁷

¹Harbor Branch Oceanographic Institute, Florida Atlantic University, 5600 US 1 N, Ft. Pierce, FL 34946,
USA

²Department of Oceanography, University of Hawaii, 1000 Pope Road, Honolulu, HI 96822, USA

³Scripps Institution of Oceanography, University of California San Diego, 9500 Gilman Dr., La Jolla, CA
92093, USA

⁴Department of Marine Chemistry and Biogeochemistry, Woods Hole Oceanographic Institution, Woods
Hole, MA 02543, USA.

⁵Ocean and Earth Science, National Oceanography Centre, University of Southampton, Southampton, UK

⁶NOAA Fisheries, Antarctic Ecosystem Research Division, 8901 La Jolla Shores Dr., La Jolla, CA 92037,
USA

⁷College of Environmental Science, University of Massachusetts Boston, 100 Morrissey Blvd, Boston,
MA 02125, USA

To be submitted to Deep-Sea Research I

December 10, 2018

* Corresponding author, email: jiangm@fau.edu, Telephone: 001-772-242-2254.

Abstract

The Antarctic Peninsula (AP) shelf is an important source of dissolved iron (Fe) to the upper ocean in the southern Scotia Sea, one of the most productive regions of the Southern Ocean. Here we present results from a four-year (2003-2006) numerical simulation using a regional coupled physical-biogeochemical model to assess the Fe sources and transport on the AP shelf and toward the southern Scotia Sea. The model was validated with a suite of data derived from *in situ* surveys and remote sensing. Model results indicate that sediments in the AP shelf and the South Orkney Plateau (SOP) provide the dominant source of shelf-derived Fe, broadly defined as Fe from the continental shelf and slope, to the upper 500 m in the southern Scotia Sea. Additional Fe inputs to the region are associated with the Antarctic Circumpolar Current (ACC) and the northern limb of the Weddell Gyre, deep-ocean sediment sources, dust deposition, and icebergs. Fe on the AP shelf originates primarily from sediments on the relatively shallow inner shelf and is directly injected into the water column and transported toward Elephant Island by the confluent shelf currents. Off-shelf Fe export is primarily through entrainment of shelf waters by the ACC's Southern Boundary frontal jet along the northern edge of the AP shelf, the Hesperides Trough, and the SOP shelf. About 70% of the export takes place below the surface mixed layer, and is subsequently re-supplied to the euphotic zone through vertical mixing, mainly during austral fall and winter. The exported shelf-derived Fe is then advected downstream by the ACC and Weddell Gyre and spread over the southern and eastern Scotia Seas. Waters with elevated Fe concentration in the Scotia Sea are largely restricted to south of the Southern ACC Front.

Key words: Coupled physical-biogeochemical model, iron (Fe), off-shelf transport, shelf sediment, Antarctic Peninsula, southern Scotia Sea

1. Introduction

Iron (Fe) and light are two primary factors limiting phytoplankton blooms in the Southern Ocean (Martin et al. 1990; Mitchell et al. 1991; Nelson and Smith, 1991). Sources of Fe to the Southern Ocean euphotic zone include dust deposition, mixing input from shelf sediments, sediment release from drifting icebergs, and vertical supply driven by mixing and mesoscale eddies (e.g. Boyd et al. 2012; Tagliabue et al. 2014; Wadley et al. 2014). While the relative importance of each source may depend on the specific area under consideration, sediment input from the Antarctic continental shelves is hypothesized to be the dominant Fe source to the open waters of the Southern Ocean (Lancelot et al. 2009; Boyd et al. 2012; Wadley et al. 2014).

The region of the Antarctic Peninsula (AP), southern Drake Passage and southern Scotia Sea (Figure 1) is one of the most productive in the Southern Ocean (Kahru et al. 2007; Arrigo et al. 2008). Recent studies have demonstrated that Fe from AP shelf sediments is an important source to the southern Drake Passage and Scotia Sea (Hopkinson et al. 2007; Dulaiova et al. 2009; Ardelan et al. 2010; Hatta et al. 2013; Measures et al. 2013; Wadley et al. 2014). The transport mechanism of shelf-derived Fe, however, remains to be fully understood, and may involve several steps. These include deep winter mixing, which can entrain Fe from shelf sediments to the overlying water column; subsequent shelf transport converging toward Elephant Island; off-shelf export from that area; and finally downstream transport (Dulaiova et al. 2009; Zhou et al. 2010; Jiang et al. 2013b; Measures et al. 2012, 2013; Wadley et al. 2014).

Fe fluxes from AP shelf sediments and the subsequent off-shelf export are poorly quantified. It is generally believed that the dominant sediment Fe sources in the area are from the western AP to the South Shetland Islands (SSIs) (Dulaiova et al. 2009; Jiang et al. 2013b; Measures et al. 2012, 2013; Annett et al. 2015). Dulaiova et al. (2009) provided the first estimate

of off-shelf Fe export between Livingston Island and Elephant Island, $\sim 1.1 \times 10^5$ mol/day, based on measurements of surface dissolved Fe and radium isotopes during an austral summer cruise. Subsequently, Hatta et al. (2013) estimated that the cross-shelf transport is about 1.4×10^5 mol/day for the upper 100 m during winter 2006. Using a relatively simple Fe model coupled with an eddy-resolving global model, Wadley et al. (2014) estimated that the majority of surface dissolved Fe in the Southern Ocean is derived from shelf sediments, estimated to sustain up to 75% of the regional productivity. No specific estimates of Fe fluxes, however, were provided in that work.

Recent studies have illustrated the major transport pathways of surface waters around the AP shelf, and from the shelf and Weddell Sea toward the southern Scotia Sea and South Georgia (e.g. Fach et al., 2006; Zhou et al. 2006; Thompson et al. 2009; Jiang et al. 2013b; Thompson and Youngs, 2013; Youngs et al. 2015). On the northern AP shelf, the Antarctic Coastal Current and southern Bransfield Strait Current typically flow southwestward toward the western end of the Bransfield Strait, where they meet the northward-flowing Gerlache Strait Current to form the Bransfield Strait Current (BSC), which is directed along the southern slope of the SSIs toward Elephant Island (von Gyldenfelt et al. 2002; Zhou et al. 2002, 2006). On the outer (northern) slope of the South Shetland Islands shelf, the Antarctic Circumpolar Current's (ACC) Southern Boundary (SBdy) flows through the Shackleton Fracture Gap, with a portion intruding onto the Bransfield Strait and combining with the BSC to reach the Elephant Island shelf. Here, these combined shelf flows interact with a branch of the ACC, resulting in a strong and persistent off-shelf transport of Fe-rich shelf waters (Zhou et al. 2010, 2013; Jiang et al. 2013b). Further east, Weddell waters spillover through the Hesperides Trough, between Elephant Island and the South Orkney Plateau (SOP), onto the southern Drake Passage (Heywood et al. 2004; Thompson and

Heywood, 2008). Most of the Weddell waters, however, exit the basin following the Weddell Front, which skirts the southeastern flank of the SOP. Both of these transports may carry significant Fe, despite the relatively low dissolved Fe levels present in the Weddell waters (Hatta et al. 2013). Yet the Fe fluxes associated with these pathways have not been quantified.

After leaving the AP shelf, the shelf-derived Fe is transported downstream into the southern Scotia Sea by the Southern ACC Front (SACCF) and SBdy (Zhou et al. 2010; Frants et al. 2013b; Jiang et al. 2013b). The relative proportion of Fe supply between these two currents has not been quantified. Recent studies suggested that organic Fe ligands and particulate phases of Fe may play an important role in stabilizing dissolved Fe and hence facilitating its long distant transport toward downstream, as indicated by the long-distant Fe transport from hydrothermal vents in the deep South Pacific Ocean (e.g. Fitzsimmons et al. 2014, 2017). Based on an analysis of surface drifter trajectories and chlorophyll responses in the southern Scotia Sea to the inter-annual variability of frontal positions, Thompson and Youngs (2013) argued that the SACCF acts as a barrier to Fe transport, such that high surface chlorophyll is associated with the area south of SACCF. This is consistent with the remote sensing results reported by Kahru et al. (2007) and modeling results by Wadley et al. (2014).

In this manuscript, we present results of a modeling investigation of the origin and fate of Fe inputs to the AP shelf and the southern Scotia Sea. Our study employs a high-resolution regional circulation model (Jiang et al. 2013b), coupled with a biogeochemical model of intermediate complexity that includes detailed representations of major Fe cycling and Fe-ligand dynamics (Jiang et al. 2013a). The objectives are: (a) to investigate the detailed transport pathways, both surface and subsurface, of shelf-derived Fe from the AP to the southern Scotia Sea; (b) to quantify the Fe fluxes associated with these pathways; and (c) to assess the

contributions of these shelf-derived Fe sources to the Fe budget of the southern Scotia Sea. We focus on the uppermost 500 m, which is most relevant to the control of primary productivity in the southern Scotia Sea.

2. Methods

2.1. Physical model

The physical model is based on that described by Jiang et al. (2013b), with some modifications as detailed below. The model domain spans the AP, Drake Passage, Scotia Sea, northern Weddell Sea, and South Georgia. A portion of the model bathymetry and grid is shown in Figure 1. The model grid has its highest resolution (~ 2 km) on the AP shelf and slope, a moderately high resolution (~ 5 km) in the southern Drake Passage and Scotia Sea, and relatively coarse resolution (~ 10 km) in the northern part of the domain. The model is based on the Regional Oceanic Modeling System (ROMS), which is a terrain-following S-coordinate modeling system (Shchepetkin and McWilliams, 2005). There are 40 vertical layers, allowing for the structure of vertical grid thickness to vary, with a nearly uniform distribution in shelf areas and surface-condensed distribution in deeper areas. A Smagorinsky-type representation of mixing is used for horizontal viscosity and diffusivity (Smagorinsky, 1963), in which the viscosity is computed from current shear and grid size, and diffusivity is set to be the same as the viscosity. On the AP shelf, the modeled viscosity and diffusivity are on the order of $10 \text{ m}^2 \text{ s}^{-1}$, which is the same order as projected by Okubo (1971) with a horizontal scale of 2-3 km. A second-order algorithm is used to compute the pressure-gradient term in order to minimize the so-called sigma-coordinate truncation error (Shchepetkin and McWilliams, 2003). Vertical mixing is computed using the non-local K-profile vertical mixing scheme (KPP) (Large et al.,

1994). No tidal mixing is explicitly simulated in the model. Instead, tidal mixing is accounted for by scaling the mixing rate computed from the KPP scheme inversely with distance to the bottom.

The model is initialized with the climatological temperature (T) and salinity (S) from the World Ocean Atlas 2009 (WOA09) (Antonov et al., 2010; Locarnii et al., 2010), spun-up for four years using forcing data for the period 2003-2006, and then run for a further four years using the same forcing. In contrast to the previous simulation described by Jiang et al. (2013b), the meteorological forcing (except humidity and precipitation) is derived from the ECMWF 3-hour ERA-interim global reanalysis (Dee et al. 2011). Sea surface temperature (SST) and sea surface salinity (SSS) are derived from the global HYCOM 1/12° model (<https://hycom.org/global>), and relative humidity and precipitation are from the long-term (1987-2006) monthly mean of Hamburg Ocean Atmosphere Parameters and Fluxes from Satellite Data (HOAPS) (Andersson et al., 2010). A bulk formulation from the NCAR Community Climate System Model (CCSM) is used to compute the wind stresses and heat fluxes from surface winds and other meteorological parameters (Collins et al., 2006). To reduce uncertainty associated with surface heat and salt fluxes, surface temperature and salinity are restored to HYCOM SST and SSS with a variable time scale for temperature dependent on ocean heat sensitivity, and a fixed 10-day time scale for salinity, respectively. The model open boundary conditions of temperature, salinity, currents, and sea level, were derived from the global HYCOM 1/12° model output with a 3-day interval.

The model has a fully integrated sea-ice sub-model based on a combination of the elastic-viscous-plastic (EVP) rheology (Hunke and Dukowiz, 1997; Hunke, 2001) and simple one-layer ice and snow thermodynamics with a molecular sub-layer under the ice (Mellor and Kantha, 1989). The open boundary conditions for the sea-ice module include ice thickness, ice

concentration, and snow thickness, all of which are derived from multi-year mean output from the $\frac{1}{4}^\circ$ global OCCAM model (Webb et al. 1998). Ice temperature is fixed at -15°C .

2.2. Biogeochemical model

The biogeochemical model is the Southern Ocean Fe model (SOFe), which has 18 components representing the basic functions of lower trophic food-web and the key biogeochemical processes involved in the Southern Ocean ecosystems (Figure 2, Jiang et al. 2013a). The model describes the cycling of three types of nutrients: nitrogen (N), silicon (Si), and Fe. The nitrogen cycle includes phytoplankton uptake, zooplankton grazing, and microbial loop processes. Nutritional nitrogen is split into two pools: nitrate (NO_3) and ammonia (NH_4). There are three Si pools: siliceous acid (silicate, $\text{Si}(\text{OH})_4$), diatoms, and biogenic silica (BSi), and it is assumed that the grazers do not contain any silicon in their cells. There are two phytoplankton groups: large ($>5\ \mu\text{m}$) and small ($<5\ \mu\text{m}$) phytoplankton. The parameterization of phytoplankton photosynthesis follows the formulation by Platt et al. (1980). There are also two zooplankton groups representing micro-zooplankton and meso-zooplankton, with micro-zooplankton grazing upon bacteria, small phytoplankton and large phytoplankton, and meso-zooplankton grazing upon large phytoplankton and micro-zooplankton. The meso-zooplankton group includes krill without specifically modeling their life cycle and migration behaviors. The model also includes a microbial loop by explicitly simulating heterotrophic bacteria (B) and separating detritus into dissolved organic nitrogen (DON) and particulate organic nitrogen (PON). Bacteria consume ammonia, DON and PON, while being prey for micro-zooplankton. The bacterial uptake of nitrogen follows the formulation by Anderson and Williams (1999).

The model explicitly simulates the Fe cycle with 5 components representing dissolved

1 inorganic Fe (Fe'), Fe bound to strong and weak organic ligands (FeL1 and FeL2), colloidal Fe
2 (FeC), and particulate Fe (FeP). In this manuscript, dissolved Fe includes all 4 dissolved Fe
3 species (Fe', FeL1, FeL2 and FeC). The model also explicitly simulates Fe ligand dynamics by
4 including two types of Fe-binding ligands, strong (L1) and weak (L2) ligands, which are
5 produced by bacteria and remineralization of particulate organic carbon (Trick, 1989; Barbeau et
6 al. 2001; Boyd and Ellwood 2010; Gledhill and Buck, 2012). No ligand production due to
7 phytoplankton growth or zooplankton grazing is included (e.g., Barbeau et al., 1996; Sato et al.,
8 2007). The key ligand processes include bio-complexation, photo-degradation, thermal
9 dissociation, and ligand production. This Fe model has been tested with a 1-D model for the SSI
10 shelf (Jiang et al. 2013a) and for the California Current system using laboratory incubation data
11 (Bundy et al. 2016).

12 To accommodate changes from the 1-D simulation by Jiang et al. (2013a) to the 3-D
13 simulation in this study, some modifications of model parameters have been made (see Table 1).
14 The main changes include an increase in small phytoplankton growth, which permits an increase
15 of phytoplankton productivity overall, and adjustments to several zooplankton grazing
16 parameters (e.g., half saturation constants, grazing preferences) to optimize the simulation of
17 phytoplankton proportions between the two groups (Jiang et al., manuscript in prep.).

19 **2.3. Fe inputs**

20 External Fe inputs to our study area include dust deposition, sediment fluxes, and
21 horizontal boundary inputs from upstream. In this simulation, we did not directly include Fe
22 contribution from iceberg, which have been shown to be a significant factor in the Fe budget in
23 the area (e.g. Wadley et al. 2014). We did not directly simulate sea ice Fe either. Although sea

ice mainly derives Fe from seawater, our model omits the sea ice-mediated re-distribution of surface Fe over time and space, which may create some bias in surface Fe distribution and productivity. The atmospheric Fe input is derived from the monthly dust deposition predicted from an atmospheric model, assuming dust contains 3.5% Fe and that its solubility is 2% (Luo et al. 2005; Mahowald et al. 2005).

As there are no direct measurements of sediment Fe fluxes for the AP shelf, we chose a simple depth-dependent formulation,

$$F = C * \frac{50}{\max(50, h)}, \quad (1)$$

where C is a constant that equals $16 \times 10^{-5} \mu\text{mol m}^{-2} \text{s}^{-1}$ for the entire model domain, except in the Weddell Sea where $C = 1 \times 10^{-5} \mu\text{mol m}^{-2} \text{s}^{-1}$. Assuming a characteristic water depth of 200 m for continental shelves, the resulting sediment flux amounts to $3.45 \mu\text{mol m}^{-2} \text{day}^{-1}$ on the AP shelf and $0.35 \mu\text{mol m}^{-2} \text{day}^{-1}$ at 2000 m. But it is only $\sim 0.2 \mu\text{mol m}^{-2} \text{day}^{-1}$ on the northwest Weddell shelf. The choice of constant C was manually adjusted and therefore is somewhat subjective. Yet our results indicate reasonably good agreement between the modeled Fe concentrations and the measurements from the two research cruises conducted in the AP region within the same model period, as well as data from a cruise in the Scotia Sea and South Georgia (detailed below). This formulation is similar to that used by Wadley et al. (2014), which entailed an empirical fit to the water depth of pore water sediment flux measurements reported by Elrod et al. (2004). A comparison between these two curves is shown in Figure 3a. The fitted flux was $3.54 \mu\text{mol m}^{-2} \text{day}^{-1}$ at 200 m and $< 0.8 \mu\text{mol m}^{-2} \text{day}^{-1}$ in areas deeper than 2000 m. In comparison, Moore and Braucher (2008) used a constant flux of $2 \mu\text{mol m}^{-2} \text{day}^{-1}$ for the entire global ocean. Overall, our sediment flux on the shelves (except for the northwest Weddell shelf) is comparable to that used by Moore and Braucher (2008) and Wadley et al (2014).

In order to provide open boundary condition for dissolved Fe, we used an empirical formulation based on the dissolved Fe concentration measured at two stations within the ACC during an austral summer 2004 cruise (Zhou et al. 2010; Measures et al. 2013). These waters are presumably not affected by the Fe input from the AP shelf, and thus should provide adequate background information on boundary water properties, including Fe and nutrients. The dissolved Fe concentration at these stations is strongly correlated with the silicate concentration with the following relationship ($r=0.88$, $p<0.01$; Figure 3b),

$$Fe_{bg} = 0.0701 e^{0.0194Si(OH)_4} \quad \text{if water depth} < 1000 \text{ m}, \quad (2)$$

where 1000 m is the depth limit of the bottle samples. We assumed that $Fe_{bg}=0.4$ nM for all depths >1000 m. This formulation was applied to all of the open boundaries and was used to set the initial Fe condition for the entire model domain including the Weddell Sea. Therefore, the shelf-derived Fe can be broadly defined as $Fe - Fe_{bg}$, which also includes contribution from slope sediment.

2.4. Data

The physical model has been previously calibrated, focusing on the AP shelf region, with available climatological data and field measurements from two cruises (Jiang et al. 2013b): the LMG0402 cruise in February 12-March 24, 2004 and the NBP0606 cruise in July 3-August 15, 2006. LMG0404 took place along the northeast of Elephant Island, whereas NBP0606 surveyed three transects across the northern AP shelf (Zhou et al. 2010, 2013; Hatta et al. 2013; Measures et al. 2013). In this manuscript, we present further comparisons with additional remote sensing and *in situ* survey data, particularly dissolved Fe and surface chlorophyll observations, to gauge the model performance. The following data sets (Table 2) were used: (1) sea surface height

(SSH) from the AVISO satellite altimetry products, derived from merged measurements by several satellites (<http://www.aviso.oceanobs.com/>); (2) observed T, S, nutrient (nitrate and silicate) concentrations, and dissolved Fe concentration during the two cruises noted above (Hatta et al. 2013; Measures et al. 2013, Zhou et al. 2010, 2013); (3) surface chlorophyll concentration derived from MODIS satellite data (Kahru et al., 2007); (4) all of the available trajectories of surface drifters released around the AP in the last three decades, including those released by the Antarctic Marine Living Resources (AMLR) and by the British Antarctic Surveys (<http://www.aoml.noaa.gov/phod/gdp/>; Thompson et al. 2009; Thompson and Youngs, 2013; Reiss and Jiang, 2018, manuscript in prep.); (5) surface mixed-layer depth (MLD) estimated from the global Argo float data set (Dong et al., 2008); (6) vertical mixing rates estimated based on hydrographic and velocity measurements along three transects across the Drake Passage and Scotia Sea, one transect along the North Scotia Ridge, and one transect along the South Scotia Ridge, obtained in 1993-1999 (Naveira Garabato et al., 2004); and (7) Fe, T, and S measurements from a British Antarctic Survey cruise across the SOP, the southern Scotia Sea and South Georgia waters during austral spring (October 24-December 3, 2006) (see Table 2 in Nielsdóttir et al., 2011).

3. Results and discussion

3.1. Model performance

In order to assess the model skill, the following quantitative metrics were computed: (1) point-to-point correlation, (2) root-mean-squared-error (RMSE), and (3) mean difference between model and observed values (Table 2). Unless specifically noted, all of the model results were taken from monthly means of the months closest to the field observations. Spatially, model

outputs were matched with observational data by interpolating onto the sample locations and depth or the remote sensing grid.

3.1.1 Physical characteristics

Model predictions of the general horizontal and vertical structures of temperature and salinity were validated with hydrographic observations from the LMG0402 (austral summer) and NBP0606 (austral winter) cruises, similarly to the validation carried out by Jiang et al. (2013b). Results show a strong agreement between the model and observations, with one-to-one correlation coefficients $r > 0.84$ ($p < 0.01$) for both temperature and salinity, and RMSE of 0.54°C for temperature and < 0.1 psu for salinity, respectively. In addition, the linear regression of model output to observed data yields a slope of 0.77 for T and 0.93 for S during the LMG0402 cruise, and a slope of 0.88 for both T and S during the NBP0606 cruise, indicating an under-estimation of spatial gradients of T and S.

To gauge the skill of model predictions of the regional circulations and ACC frontal dynamics (particularly as regards the SACCF and SBdy), we compare the modeled SSH with AVISO SSH for subsets of the simulation period (2003-2006). An example of this comparison is shown in Figure 4a, b for August 2006. In general, the model is able to accurately reproduce the observed SSH spatial pattern, particularly the intense northwest to southeast gradient representing the ACC fronts. A point-to-point comparison yields a correlation coefficient $r = 0.94$ ($p < 0.001$). Both the model and AVISO frontal positions closely track the climatological ACC frontal positions determined by Orsi et al. (1995), except in the central Scotia Sea, where the SACCF takes a more direct course toward South Georgia before veering around and closely hugging the island. This is consistent with results from recent studies (e.g., Kim and Orsi, 2014),

1 which suggest a more direct route of the SACCF than in the Orsi et al. (1995) climatology.
2 However, the model did not capture the southward meandering of the Polar Front (PF) south of
3 Cape Horn. Instead, the modeled PF largely joins the Sub-Antarctic Front (SAF), following the
4 continental slope off Cape Horn. This is likely due to the model's bias created by the terrain-
5 following vertical coordinate system, which tends to produce significant error in the horizontal
6 pressure gradient term over steep topography (Song and Haidvogel, 1994; Shchepetkin and
7 Williams, 2003). To minimize this error, a high horizontal resolution is needed. Yet this model
8 has a relatively coarse horizontal resolution in that area (~10 km).

9 We also compared the temporal evolution of modeled and observed SSH along a transect
10 that runs from the northwestern Weddell Sea through the Hesperides Trough to southern Drake
11 Passage, for which a uniform offset of 1.7 m is applied to the AVISO SSH (Figure 4c; see Figure
12 4b for the transect location). The modeled SSH along this transect agrees strongly with data for
13 both mean and variance with $r=0.98$ ($p<0.01$) and 0.96 ($p<0.01$), respectively, for the 4-yr (2003-
14 2006) model period. Note that the model predicts a stronger SAF than indicated in the AVISO
15 data, as reflected in the higher SSH gradient at around 58°S. The model also reproduces well the
16 dominant periods of SSH oscillations (Jiang et al., manuscript in prep.).

17 Satellite SSH does not adequately resolve the circulation on the AP shelf and in the
18 Weddell Sea due to the winter sea ice coverage, the relatively weak prevailing currents, and the
19 small baroclinic Rossby radius. Thus, to further validate the model, we compared the trajectories
20 of surface drifters (<http://www.aoml.noaa.gov/phod/gdp/>) in the area with those of simulated
21 neutrally buoyant particles released from the AP shelf. These trajectories also illustrate the
22 connectivity of Antarctic krill between the AP shelf, Scotia Sea and South Georgia (e.g. Fach et
23 al. 2006; Thorpe et al. 2007). Unlike surface drifters, however, modeled particles are allowed to

1 move vertically. We do not expect significant bias because the vast majority of the modeled
2 particles remain within the surface mixed layer. The trajectories of modeled particles were
3 computed using the built-in Lagrangian tracking program in ROMS (Piñones et al. 2013a, b),
4 which takes into account advection and vertical mixing.

5 Figure 5 shows a comparison of the trajectories of the modeled particles, continuously
6 released between July 1 – August 31, 2006, and those of surface drifters released from or passing
7 through the AP shelf until the end of 2017. The patterns of these trajectories agree well. The
8 trajectories of modeled particles released during other periods show very similar patterns.
9 Overall, most particles except those released in the northwestern Weddell Sea converged toward
10 the Elephant Island shelf/slope area, by either transiting through the gap between Elephant and
11 Clarence Islands, or through the Shackleton Fracture Gap over the northern Elephant Island slope.
12 Particles originating in the northwestern Weddell Sea generally crossed the western end of
13 Hesperides Trough, where they were entrained offshore and downstream by the ACC currents. A
14 subset of particles was advected around the Powell Basin, following the Antarctic Slope Front
15 and the Weddell Front. These are consistent with previous studies using surface drifters (Zhou et
16 al. 2006; Thompson et al. 2009; Thompson and Youngs, 2013; Youngs et al. 2015), field
17 measurements (e.g. Heywood et al. 2004; Zhou et al. 2010, 2013) and numerical models (Jiang et
18 al. 2013b). Once in the open ocean, these particles and drifters scattered downstream through the
19 Ona Basin and the southern Scotia Sea, but largely bypassed the eastern Scotia Sea and South
20 Sandwich Islands. The SACCF appears to define the northern limit of these particles and drifters,
21 with only a few being able to cross the SACCF and pass through the central Scotia Sea.

22 Vertical mixing is critical to correctly model the Fe supply from the shelf sediment to the
23 overlying water column, as well as the vertical Fe supply in the open ocean (Frants et al. 2013a).

Here we compare modeled vertical mixing with that estimated by Naveira Garabato et al. (2004). Since we do not have estimates of vertical mixing during the model period, this comparison is not optimal. The modeled mixing was chosen from the monthly mean in January 2006. Results from other months are similar, except for austral winter, when surface mixing is much stronger. Further, the comparison is limited to values below the surface mixed layer. We grouped the data into 4 areas: (1) Drake Passage, (2) North Scotia Ridge, (3) South Scotia Ridge including the AP and SOP shelves, and (4) the southern Scotia Sea. The modeled mixing rates exhibit profiles similar to those from observational estimates, but the modeled rates are smaller by a factor of about 2-3 relative to estimates from the field measurements in the Drake Passage and the North Scotia Ridge areas except for the top 200 m in the Drake Passage (Table 2, Figure 6). In particular, the model underestimates the vertical mixing rates in the southern Drake Passage, where strong upwelling and ventilation take place as a result of strong westerly wind forcing (e.g. Russell et al. 2006), and in areas where strong bathymetric features lead to elevated mixing by lee waves and internal tides (e.g., the North Scotia Ridge) (Naveira Garabato et al. 2004; Padman et al. 2006; Heywood et al. 2007). Modeled and observation-based mixing rates are, however, in good agreement for the South Scotia Ridge (including the AP shelf) and southern Scotia Sea areas, which are the focus of this study, particularly within the top 500 m (Table 2, Figure 6).

The surface MLD represents an important parameter that is closely tied to the primary productivity in this region (Mitchell et al. 1991). Therefore, we also validated the modeled MLD by comparing model output with the climatological mean MLD derived from Argo float data by Dong et al. (2008) (Table 2). In winter, the modeled MLD exhibits a similar pattern to observations, with a deep MLD in the northwestern Drake Passage, a moderate MLD along the rest of the ACC path, and a relatively shallow MLD in the southern Scotia Sea and around the

1 South Sandwich Islands. The modeled MLD, however, is significantly shallower than the
2 estimated MLD in the northwestern Drake Passage area in which the Antarctic Intermediate
3 Water and Sub-Antarctic Mode Water reside. In summer, the modeled MLD shows a good
4 agreement with that from Dong et al. (2008), both in terms of spatial pattern and overall values.
5 The modeled MLD in the southern Scotia Sea is ~30-50 m, similar to previous estimates based
6 on *in situ* density profiles (e.g. Mitchell et al. 1991).

7 We also compared the modeled MLD with the MLD estimated from the T and S profiles
8 measured in winter 2006 (NBP0606) and summer 2004 (LMG0402) surveys using the same
9 density threshold criterion of 0.03 kg/m^3 (Mitchell et al. 1991; Dong et al. 2008). A point-by-
10 point comparison between modeled and observed MLD yields no significant correlation for the
11 summer cruise data, but a weak ($r=0.29$, $p<0.01$) correlation for the winter data. This is because
12 the modeled MLD is quite uniform across the area of the stations, which contrasts with a
13 significant spatial gradient in the observed MLD during both cruises. In particular, a strong
14 meridional gradient was observed during the winter 2006 cruise, with deep mixing down to the
15 shelf floor in the southern Bransfield Strait. The mean modeled MLD for both survey periods,
16 however, is comparable to the observed MLD ($36.7 \pm 0.5 \text{ m}$ versus $40.8 \pm 15.7 \text{ m}$ in summer 2004,
17 and $84.1 \pm 22.0 \text{ m}$ versus $84.8 \pm 49.0 \text{ m}$ in winter 2006) (Table 2).

19 **3.1.2 Dissolved Fe concentration**

20 Figure 7 shows a comparison between the modeled and observed dissolved Fe
21 concentration during the summer 2004 (LMG0402) cruise. Modeled Fe displays an elongated
22 pattern, with high Fe concentration extending from the SSIs to Elephant Island, where a high Fe
23 tongue is seen extending toward the Shackleton Traverse Ridge. This is broadly in agreement

with the measurements, which were, however, limited to the slope and ACC waters. The modeled and observed mean Fe profiles agree within statistical error, both indicating a nearly uniform vertical distribution of Fe concentration below 200 m and a clear reduction toward the surface (Figure 7c). The spatial variability between 100-500 m is, however, much larger, mainly due to the horizontal gradient of dissolved Fe concentration (Figure 7a-c). On average, the model somewhat overestimates the surface Fe concentration. A point-to-point comparison also indicates significant correlations between model and data for surface only ($r=0.6$, $p<0.01$) and all available data ($r=0.52$, $p<0.01$) (Table 2; Figure 7d-e).

A similar comparison for the winter 2006 (NBP0606) cruise also shows a good agreement between the model and observed Fe concentrations (Figure 8). The cruise surveyed three transects across the western and middle Bransfield Strait and near Elephant Island (Figure 8g). Both the modeled and observed fields indicate high dissolved Fe concentration along the western Bransfield Strait transect, with dissolved Fe decreasing rapidly northward from the coastline (Figure 8a, b). High Fe concentration is found over the northern South Shetland shelf, and moderate values within the Bransfield Strait (Figure 8c, d), with the former likely due to local sediment input and the latter resulting from both transport from the western Bransfield Strait by the BSC and local sediment flux. In the top 200 m, the model overestimates Fe values in the northern South Shetland Islands shelf, but underestimates Fe values in the Bransfield Strait. Along the Elephant Island transect, both modeled and observed Fe distributions show maximum concentrations surrounding Elephant Island, likely due to the converging transport from the western AP shelf (Figure 8e, f; Jiang et al. 2013b). The model also shows moderately high Fe concentrations (~ 1 nM) over the northern Weddell slope, which is comparable to the measured values. Sañudo-Wilhelmy et al. (2002) reported the surface Fe concentration at 15 stations over

the slope of the northwestern Weddell Sea in February-March, 1991. Their values ranged from 0.53 to 2.15 nM, similar to our measurements and model results.

Viewed together, the vertical profiles of modeled and observed Fe concentration also agree well both in the mean values and the ranges, except that the model slightly underestimated the dissolved Fe concentration in the top 300 m (Figure 8h). Both modeled and observed profiles indicate generally higher Fe concentrations in the upper 500 m than in the deeper areas. This is consistent with the concept that deep winter mixing leads to full ventilation of shelf waters, and hence strong Fe input from the shelf sediment (Hatta et al. 2013; Measures et al. 2013). A point-by-point comparison also indicates strong correlations between the modeled and observed Fe distributions for both the surface ($r=0.77$, $p<0.001$) and for the entire water column ($r=0.80$, $p<0.001$) (Table 2; Figure 8i, j).

We also compared the model output in the Scotia Sea with the measurements of T, S, and dissolved Fe concentrations in November 2006 by the British Antarctic Survey (Table 2; Nielsdóttir et al., 2011). Overall, modeled T and S agree very well with observations, with point-to-point correlation coefficient $r=0.88$ ($p<0.01$) and $r=0.96$ ($p<0.01$), respectively. However, the model underestimates the water temperature by 0.23°C. The modeled Fe concentration correlates with data reasonably well ($r=0.76$, $p<0.01$) across all of the stations. Overall, however, the modeled Fe concentration is higher than observed (0.61 ± 0.30 vs 0.35 ± 0.50 nM). At the station on the SOP, modeled Fe is nearly constant vertically at ~ 1.5 nM, whereas the observed Fe increases from 1 nM at 50 m to ~ 2 nM below 200 m.

3.1.3 Surface chlorophyll concentration

In order to assess the realism of the modeled primary productivity, which represents the Fe removal term in the surface Fe budget, modeled surface chlorophyll concentration was also validated with the MODIS observations. As an example, here we show comparisons of modeled and observed surface chlorophyll in October 2005, January 2006, and April 2006, which represent the seasonal patterns of austral spring, summer and fall (Figure 9). Both modeled surface chlorophyll and MODIS images show a broad band of phytoplankton blooms extending from the AP shelf into the southern Drake Passage and southern Scotia Sea, and the highly productive areas over the Argentinean shelf and around South Georgia. Surface chlorophyll in all of these areas exhibits a strong seasonal cycle, with a distinct peak in summer. The modeled chlorophyll concentration, however, is higher than observed on the AP shelf. During austral summer, both modeled and satellite data indicate significant phytoplankton blooms in the northern Weddell Sea (Figure 9c, d). This area is, however, often covered by heavy clouds, such that high quality satellite images of surface chlorophyll are rare. Thus, there is substantial uncertainty in the satellite composites, and caution needs to be taken in making a direct comparison with the model output. Comparisons for other months or years show similar levels of agreement between the model and observations (not shown). Modeled average chlorophyll in four key areas (AP shelf, Polar Frontal Zone, Scotia Sea and northern Weddell Sea) also agree well with data both seasonally and inter-annually (Jiang et al. 2018, manuscript in prep.).

3.2. Fe sources and spatial distribution

The model results show high dissolved Fe concentration on the AP shelf, particularly in shallow areas complex bathymetry, the SOP shelf, and the southern Scotia Sea, largely following the dispersive path of the SBdy. This clearly indicate that the key areas of Fe sources to the AP

shelf are the western part of the AP shelf, the South Shetland Islands shelf, and the southern Bransfield Strait shelf, where the dissolved Fe concentration is > 2 nM throughout the year as seen in Figure 10. This is broadly consistent with previous studies (Dulaiova et al. 2009; Hatta et al. 2013; Measures et al. 2013; Wadley et al. 2014; Annett et al. 2015, 2017). In particular, Wadley et al. (2014) predicted similar spatial patterns. On the inner shelf, observations, by the Palmer Long-term Ecological Research (LTER) program on the western Antarctic Peninsula shelf, also show a strong cross-shelf gradient with high dissolved Fe (> 3 nM) (Annett et al. 2017). North of the South Shetland and Elephant Islands, offshore entrainment of shelf-derived Fe extends as far north as 58°S , near the Polar Front, with dissolved Fe concentrations of ~ 0.3 - 0.6 nM between 0-600 m.

The vertical distribution of Fe on the AP shelf is rather uniform both in the summer and winter except the relatively low value within the top 100 m due to surface biological removal. Overall (Figures 8, 10), During winter time, Fe concentration within the top 400 m is higher than deeper area, consistent with the notion that shelf sediment provides more Fe input (Figures 10, 11a; Hatta et al. 2013; Measures et al. 2012, 2013). This near-uniformity in vertical Fe distribution in the source areas is also reflected in the vertical Fe distribution downstream, which shows two distinct bands of elevated dissolved Fe concentration associated with the SBdy and SACCF, respectively (Figure 11b). The cores of these bands reside between 100-1000m, indicating the influence of the shelf-derived Fe on the southern Scotia Sea waters is mainly limited to the top 1000 m or so.

While sediment inputs to the water column take place throughout the year, the dissolved Fe flux over most of the deeper shelf areas only reaches the surface layer through deep winter mixing. During the summer months, the modeled MLD is shallow only at about 50 m on the

shelf and in the southern Scotia Sea. Biological removal and weak vertical mixing lead to a clear reduction of dissolved Fe in the surface layer, as shown in the observed mean profile (Figure 7c). Below the surface mixed layer, both the horizontal and vertical distributions of dissolved Fe in summer are similar to the winter distributions (not shown). In contrast, during the winter, the surface mixed layer on the AP shelf can reach between 200-500 m (Table 2; Zhou et al. 2013). Thus, a majority of the shelf areas are well mixed, and the vertical distribution of dissolved Fe on the shelves is nearly uniform as noted above. An exception to this is on the northern slope of the western Bransfield Strait, where a pronounced intrusion of Upper Circumpolar Deep Water (UCDW) into the Smith Island canyon transports warm, Fe-poor ACC waters onto the shelf and generates a stratified bottom layer with low Fe concentration (Figure 8a, b).

In the current simulation, the Fe concentration on the northwestern Weddell shelf is also moderately high, particularly in coastal areas (Figure 10). This is an area covered by seasonal sea ice and hosting significant phytoplankton blooms during summer (Figure 9c, d), which can be fueled by Fe released either from sea ice or from the shelf sediment. However, we are not aware of any direct measurements except for that of Sañudo-Wilhelmy et al. (2002), who reported a high surface Fe concentration of 10.1 nM at a station in the Antarctic Sound during March 4, 1991. The South Orkney Islands and South Georgia shelves also contribute significantly to the Fe budget in the study region that fuel phytoplankton blooms downstream (Figure 9; Venables and Moore, 2010; Nielsdottir et al. 2011). In addition, the shallow Argentinean shelf is also a clear Fe source to the overlying water column, although the regional circulation pattern acts to limit the impact of this source on Drake Passage waters (Figure 10). To constrain this source is beyond this scope of the paper, and we have no *in situ* Fe measurements in this region. While dust deposition was suggested to be significant to the phytoplankton blooms surrounding South

America (Lancelot et al. 2009; Wadley et al. 2014), more recent data in this region shows that there is no elevated value of aluminum (Al), an indicator of the dust deposition (Schlitzer et al., 2018). This suggests that the contribution of dust deposition to Fe budget in this region might be low.

The influence of the SOP and South Georgia sediments is evident in the elevated Fe concentrations surrounding those shelves (Figure 10; Wadley et al. 2014). North of the SOP, however, the influence of the AP shelf-derived Fe likely remains strong, as indicated by the high Fe core waters associated with the SBdy (Figure 11b). In the Weddell Sea, the surface Fe concentration may be underestimated, particularly during summer, because of the exclusion of the iceberg contribution (e.g. Lannuzel et al. 2008; Lin et al. 2011).

3.3. Fe transport pathways

The model results and historical studies suggest a complex yet persistent three-dimensional Fe transport pattern from the shelf sediments to the overlying water column on the AP shelf, and then from the shelf to the southern Scotia Sea, driven by winter mixing, shelf currents, and the ACC with an additional contribution from the surface Ekman transport. These transports occur throughout the year, but the fluxes and the frontal positions change seasonally and interannually. While the currents and their frontal positions on the shelf are comparatively stable seasonally, both the ACC transport and frontal positions change significantly, likely in response to the upstream forcing and surface winds (Figure 4c; Cunningham et al. 2003; Thompson and Youngs, 2013). Correspondingly, the transport pathways and volumes of dissolved Fe fluxes also change. In the summer, the surface Fe concentration is much lower than in winter, due to biological removal and reduced vertical mixing (disconnected from the high Fe

core waters). As a result, the horizontal Fe transport mainly takes place below the surface mixed layer.

On the AP shelf, deep winter mixing is likely the dominant factor controlling Fe supply to the surface layer (Hatta et al. 2013; Measures et al. 2012, 2013; Annett et al. 2017). Near-bottom vertical mixing on the shelves, however, takes place throughout the year, with tidal mixing dominating the bottom boundary layer. Much of the Fe appears to be directly injected into this boundary layer (Figure 8a, b), and is subsequently transported horizontally by shelf currents toward Elephant Island, as noted above. Much of these is then channeled through the gap between Elephant and Clarence Islands. A significant amount of Fe is also entrained into the SBdy and the shelf break current along the northern South Shetland slope and northern Elephant Island slope (Figure 12a). Importantly, a significant amount of dissolved Fe spreads offshore along the northern South Shetland slope, where the model results indicate that the SBdy veers offshore. Measurements of surface radium isotopes in summer 2006 also indicate such an offshore entrainment of shelf waters (Dulaiova et al. 2009). Significant off-shelf dispersion of dissolved Fe was also evident along the western and middle Bransfield Strait transects during the winter 2006 (NBP0606) cruise (Figure 8b, d).

Over the northwestern Weddell slope, the upper-slope portion of the Antarctic Slope Current may also transport significant dissolved Fe along the perimeter of the Powell Basin. Thompson et al. (2009) suggested that a significant influx of Weddell waters enters the Drake Passage over the South Scotia Ridge, by first overflowing the southern flank of the Hesperides Trough, then veering westward toward Clarence Island, and finally entraining into the Drake Passage across the northern flank of the trough. Our model also shows such a pathway of Fe

transport (Figure 12a). The dissolved Fe concentration associated with this flow, however, is not high, typically lower than 1 nM.

Around Elephant Island, strong off-shelf transport takes place due to vigorous interactions between the SBdy and the shelf currents (Figure 12a; Zhou et al. 2010, 2013; Jiang et al. 2013b). As the SBdy crosses through the Shackleton Fracture Gap, it frequently meanders southward and impinges upon the shelf, and then quickly returns as an off-shelf current. The bulk of this flow follows the isobaths of the continental slope northeastward toward the Terror Rise.

Further downstream, Fe transport takes place mainly through three pathways, all of which persist throughout the water column and over all seasons, although the surface transport is likely enhanced by the Ekman flow during winter (Figure 12b). The first pathway is associated with the SACCF, which flows from the shelf/slope northward along the eastern flank of the Shackleton Traverse Ridge and subsequently turns northeastward through the central Scotia Sea. The overall Fe flux along this path is relatively small, but the flow enables shelf-derived Fe to reach South Georgia, as suggested by the modeled particle and drifter trajectories (Figure 5). The second pathway is associated with the SBdy, which generally follows the northern slope of the AP and South Scotia Ridge (Figures 10 and 12). Yet a significant portion may venture into the deeper area of the Ona Basin. This flow broadly defines the northern boundary of the shelf-derived Fe export, as indicated by the dissolved Fe distribution and trajectories of surface drifters and modeled neutral particles (Figures 5 and 12). The SBdy current separates from the South Scotia Ridge slope and eventually ventures into the southern Scotia Sea between Pirie Bank and Bruce Bank. The third pathway is associated with the Weddell Slope Front, which follows the southern

flank of the SOP, then turns northeastward around the plateau, and ultimately flows northeastward toward South Georgia and the South Sandwich Islands (Heywood et al. 2004).

These Fe transport pathways can be further corroborated with the trajectories of both modeled particles and drifters (Figure 13). Both *in situ* and model experiments indicate that drifters/particles released from the northern South Shetland shelf can either follow the northern Elephant Island slope or pass through the gap between Elephant and Clarence Islands (Figure 13a, b). Few particles released in this area, however, are entrained northward along the eastern flank of the Shackleton Traverse Ridge. Consistent with the shelf circulation pattern, most particles/drifters released from the southern Bransfield Strait shelf are transported southwestward first, then cross the straits at various points to join the BSC, and eventually move through either side of Clarence Island toward the northern flank of the Hesperides Trough (Figure 13c, d). Drifters released from the northern Weddell Shelf slope generally follow the Antarctic Slope Front and transit over the South Scotia Ridge in the western Hesperides Trough toward the southern Drake Passage (Figure 13e). They then either move toward the Terror Rise to join the SACCF, or veer around the Pirie Bank toward the southern Scotia Sea. Some of the modeled particles released in these areas also follow this path (Figure 13f). A substantial fraction of the particles, however, circulate around the Powell Basin, and subsequently either skirt the SOP toward the southern Scotia Sea or exit the Powell Basin through the eastern Hesperides Trough. Both routes are consistent with modeled currents (Figure 12) and previous studies (e.g. Heywood et al. 2004; Thompson and Heywood, 2008). Youngs et al. (2015) computed the trajectories of virtual drifters based on flow fields constructed from satellite altimetry, and showed that virtual particles released from the Joinville Ridge in January 2012 almost exclusively moved around the

Powell Basin and crossed the Hesperides Trough through the eastern part of the trough toward the southern Scotia Sea.

It is useful to also examine the trajectories of particles/drifters released from the inner shelf of the western AP between Adelaide Island and Anvers Island, where high dissolved Fe concentrations are present throughout the year (Figure 10). There were only a few drifters released in this area, however, and they tended to linger for a long-time before spreading over the western AP (Figure 13g). Some modeled particles also exhibit similar trajectories. A significant portion of them, however, is able to escape from the area to move toward the southern Drake Passage and southern Scotia Sea, indicating that this is also an important source area for dissolved Fe.

3.4. Horizontal and vertical fluxes of Fe

To further quantify the contribution of shelf Fe to the Fe budget in the southern Scotia Sea, we computed the off-shelf Fe flux across a defined transect from Anvers Island to Discovery Bank. This transect spans the three major offshore transport segments: a) the northern AP shelf between Anvers Island and Elephant Island (AI-EI), b) Elephant Island to South Orkney Islands (EI-SOI), and c) South Orkney Islands to Discovery Bank (SOI-DB) (see Figure 9 for the transect locations). The location of the transect is selected such that it roughly represents the northern edge of the South Scotia Ridge. The choice of the northern edge is somewhat arbitrary, because there is no well-defined shelf edge in much of the ridge east of Elephant Island. The cross-shelf Fe flux at a specific segment is sensitive to its exact location because of the significant cross-shelf gradient of dissolved Fe concentration (e.g., Figure 12).

The choice, however, does not significantly affect our estimate of the total cross-shelf Fe flux, because most of the shelf-derived Fe in the southern Scotia Sea is from the AP shelf and the SOP.

The depth-integrated cross-shelf Fe flux is computed as

$$F = dx \int_{z_b}^0 Fe * u dz, \quad (3)$$

where u is the component of velocity directed across the transect, dx represents the grid size, dz is the thickness of a vertical layer, and z_b is the lower depth limit of the integral. For example, $z_b = -500$ m for the flux within the uppermost 500 m. The cross-shelf flux for the shelf-derived Fe can then be computed by removing the contribution of the background Fe,

$$F_{shelf} = dx \int_{z_b}^0 (Fe - Fe_{bg}) dz, \quad (4)$$

where Fe_{bg} is the background Fe concentration for open ocean waters as defined in eq. (2) (see section 2.3).

No horizontal mixing effect is included in the above flux calculation since, in the current model, the horizontal background mixing was computed based on the Smagorinsky (1963) scheme, which depends on the model grid size and velocity shear. The effective horizontal mixing coefficient around the AP shelf is ~ 30 - 100 m²/s, and we estimated that the horizontal Fe flux with this mixing rate is at least one order smaller than the advective flux.

Before discussing the cross-shelf Fe flux, it is useful to examine the vertical distributions of temperature, cross-sectional velocity, dissolved Fe concentration, and shelf-derived Fe along this transect (Figure 14). As an example, Figure 14 shows the distributions of these variables for August 2006, which indicate complex interactions between the intrusions of ACC waters (warm and low Fe) onto the shelf (negative velocity) and northward export (positive velocity) of shelf and Weddell waters (cold and high Fe). Both the export and intrusion are manifested as narrow, vertically near-uniform jets of 20-30 km width, although there is clearly strong surface Ekman

transport at this time of year, particularly along the eastern portion of the transect (Figure 14b). The influence of ACC waters is pronounced on the AP shelf and remains significant on the Elephant Island shelf. It diminishes toward the east of the SOP, where the Weddell-Scotia Confluence exerts a strong control on the circulation (Heywood et al. 2004; Thompson and Heywood, 2008).

Along the AI-EI segment, there are two major offshore export points at Anvers and Livingston Islands, which straddle the Smith Island canyon, one of the important areas of ACC intrusion onto the shelf around 63°W (e.g. Gordon and Nowlin, 1978; Capella et al. 1992; Zhou et al. 2002). Dulaiova et al. (2009) also pointed out the importance of off-shelf transport at Livingston Island. Along the EI-SOI segment, there are three strong off-shelf transport points over the northern South Scotia Ridge slope, at approximately 54°W, 51°W and 48°W, although a significant portion of the export returns toward the shelf immediately (Figure 14b). This is consistent with the results of our previous study (Jiang et al., 2013b). The first export point is a broad shelf area between 55-53°W hosting shelf waters with high Fe concentration. The waters in this area are a mixture of Bransfield Strait and Weddell Sea waters (Zhou et al. 2010; 2013). The second export point is associated with shelf waters with moderate Fe concentration (~1 nM), which are a mixture of AP shelf waters and Weddell waters crossing over the Hesperides Trough (Figures 12-14; Thompson and Youngs 2013; Youngs et al. 2015). The third point comprises a strong eastward flow through the Philip Passage, exiting the eastern end of the Hesperides Trough (Figure 14b). Further east, the Weddell Front entrains shelf-derived Fe from the SOP, following the plateau's southeastern flank toward the eastern Scotia Sea. Overall, these fluxes persist during the entire modeling period (2003-2006) but exhibit strong seasonal to inter-annual variability particularly within the upper 100 m (not shown).

The mean depth-integrated Fe export over the 4-yr simulation is shown for the entire water column (Figure 15a) and for the upper 500 m only (Figure 15b). To assess the direct contribution of shelf-derived Fe to new productivity, we also calculated the total Fe flux in the top 100 m, which roughly represents the euphotic zone in this area (see Table 3). It is clear that the contribution of background Fe to the northward Fe flux increases from the AP shelf toward the east, and it dominates the total Fe flux along the SOI-DB segments for both the entire water column and within the top 500 m. This is likely due to the dilution of shelf-derived Fe downstream and to the lack of continental shelf toward the east. The contribution of Weddell Sea-derived Fe, however, may be overestimated in the model because we initialized the Weddell Sea Fe concentration in the same manner as in other areas, yet we have essentially no data to constrain the Fe value in the Weddell deep basin. Overall, the water column within the top 100 m contributes disproportionately (~30%) to the total Fe export within the top 500 m for both total and shelf-derived Fe. This is likely due to the surface Ekman transport (northward), driven by the predominant southwesterly winds in the region (Figure 14b).

Along the AI-EI segment, shelf-derived Fe makes up ~82% of the total off-shelf Fe export throughout the water column, with a total export of 2.59×10^5 mol/day (Table 4). Even for the EI-SOI segment, shelf-derived Fe contributes >70% of the net Fe export (2.69×10^5 mol/day) within the top 500 m. Most of the export in this segment (>80%) takes place over the Elephant Island shelf between 55°-52°W (Figure 15b), where the SBdy intrudes onto the shelf and subsequently returns offshore with Fe-rich shelf waters (Zhou et al. 2010, 2013; Jiang et al. 2013b). Shelf-derived Fe in these two areas (AI-EI segment and EI shelf) combined contributes ~1.34 mol/day ($= 0.88 + 0.57 \times 0.8$) of off-shelf Fe export within the top 100 m. The total Fe export within the top 100 m from these two areas is 1.72×10^5 mol/day ($= 1.08 + 0.8 \times 0.8$). This is

about 50% larger than the estimated effective mixing flux of $\sim 1.1 \times 10^5$ mol/day estimated by Dulavoia et al. (2009), which was based on the horizontal decay rate of radium isotopes measured during January-February 2006. Using the winter 2006 (NBP0606) cruise data, Hatta et al. (2013) estimated that the Fe export from the AP shelf is about 1.4×10^5 mol/day for the upper 100 m, which is effectively the same as our multi-year mean flux. Further east, shelf-derived Fe and background Fe roughly split the Fe export at $\sim 1.2 \times 10^5$ mol/day each for the top 500 m. This flux mainly feeds into the eastern Scotia Sea and south Sandwich Islands. Altogether, shelf-derived Fe including inputs from the SOP contributes 1.68×10^5 mol/day to the top 100 m and 5.25×10^5 mol/day to the top 500 m of the southern Scotia Sea, making up $\sim 68\%$ of the total Fe flux for both layers.

The off-shelf Fe export within the top 100 m, while significant, is likely insufficient to support the high productivity in the southern Scotia Sea. The remaining Fe supply to the euphotic zone most likely stems from vertical mixing of subsurface Fe, which is either from the shelf via the horizontal transport discussed above or from deep-ocean sediments or hydrothermal vents (e.g., Frants et al. 2013a; Tagliabue et al., 2014). Internal Fe recycling in the upper ocean may also contribute to the productivity. The vertical mixing flux, however, is sensitive to the choice of depth, particularly during the summer because of the large vertical gradients of both dissolved Fe concentration and vertical mixing rate. To illustrate the vertical mixing flux, we chose 50 m for the summer (December-February) and 100 m for the winter (June-August), which are representative of the seasonal-mean MLD in the southern Scotia Sea. The resulting Fe flux due to vertical mixing from the multi-year seasonal mean is shown in Figure 16, which reveals a high flux in the southern Scotia Sea, over south Scotia Ridge, and around the South Sandwich Arc, likely due to enhanced vertical mixing by the bathymetry. In the summer months, high vertical

flux is also evident over the Shackleton Fracture Zone. The Polar Frontal Zone also shows significant vertical flux, likely due to strong mixing driven by ACC instabilities. In the southern Scotia Sea, the area of high vertical Fe flux is roughly bounded by the SACCF and the SBdy in summer. This extends southward well into the northern Weddell Sea in winter, likely due to the influence of enhanced transport of shelf-derived Fe.

3.5. An Fe budget for the southern Scotia Sea

Based on the model results and previous studies, we constructed a Fe budget of the top 100 m in the southern Scotia Sea (Table 4). For the purpose of this discussion, the area is defined as enclosed by the South Scotia Ridge in the south, Shackleton Traverse Ridge in the west, the straight line between the West Scotia Ridge and South Georgia in the north, and the line between Discovery Bank and South Georgia (33°W) in the east. Modeled new and primary productivity in this area shows large seasonal and inter-annual variations with the multi-year mean of 124.5 ± 127.1 mgC/m²/day, and 160.8 ± 159.7 mgC/m²/day, respectively. The seasonal primary productivity is 251 ± 199.1 , 313 ± 92.5 , and 72.7 ± 61.6 mgC/m²/day for spring, summer and fall, respectively, which are comparable with the satellite estimates (Arrigo et al. 2008), but 3-5 times smaller than the >1 gC/m²/day productivity rate from *in situ* measurements (Korb et al. 2012; Hoppe et al. 2017) and from a recent modeling study (Wadley et al. 2014). A typical value used in modeling studies is 2.5×10^{-5} molFe/molC (e.g. Pareh et al. 2004; Wadley et al. 2014). Hopkinson et al. (2013) reported a range from 3.7×10^{-6} to 4×10^{-5} molFe/molC under medium light conditions based on the incubation experiments during winter 2006 cruise. In the current model, we used a Fe:C ratio of 3×10^{-5} molFe/molC for phytoplankton. Therefore the average new productivity is equivalent to a Fe uptake of 311.2 ± 317.5 nmol/m²/day. Multiplying this by

1 the total area $8.25 \times 10^{11} \text{ m}^2$, the net Fe demand is estimated to be $(2.57 \pm 2.61) \times 10^5 \text{ mol/day}$ for
 2 the region (Table 4). Therefore, Fe input from the top 100m of the South Scotia Ridge shelf
 3 ($2.48 \times 10^5 \text{ mol/day}$) meets almost all of this demand. Vertical mixing at 100 m provides an
 4 additional input of about $(0.84 \pm 1.20) \times 10^5 \text{ mol/day}$. This is equivalent to 102.8 ± 145.5
 5 $\text{nmol/m}^2/\text{day}$ for the area average, about 60% more than the $64 \pm 2 \text{ nmol/m}^2/\text{day}$ the summer
 6 vertical flux estimated by Frants et al. (2013a). Cunningham et al. (2003) reported the combined
 7 baroclinic transport by the SACCF and SBdy was $9 \pm 2.4 \text{ Sv}$, and about 60% of this occurs in the
 8 top 500 m. If we add about 1 Sv of the barotropic transport to this, then the combined transport
 9 of the SACCF and the SBdy within the top 500 m is 6.4 Sv. Assuming the mean dissolved Fe
 10 concentration in the ACC waters within this layer is 0.1 nM (Figure 3b), these two currents
 11 supply an additional flux of $\sim 0.055 \times 10^5 \text{ mol/day}$, $\sim 2\%$ of the Fe demand. Additionally, dust
 12 deposition and Fe input from icebergs may also supply significant Fe to the surface layer
 13 (Lancelot et al. 2009; Boyd et al, 2012; Wadley et al. 2014). If we assume that dust and icebergs
 14 contribute 10% and 15%, respectively, the total Fe input to the euphotic zone of the southern
 15 Scotia Sea will amount to $4.07 \times 10^5 \text{ mol/day}$. The total contribution from shelf-derived Fe will be
 16 $2.25 \times 10^5 \text{ mol/day}$ ($1.68 + 0.84 \times 0.68 = 2.25$, see Table 4 with the assumption that 68% of the
 17 vertical mixing of Fe at 100 m is from shelf-derived Fe), which is $>50\%$ of the total Fe budget
 18 for the euphotic zone of the southern Scotia Sea, and more than the total Fe demand by the
 19 phytoplankton photosynthesis.

20 In the current simulation, eddy stirring is strong locally but on average its contribution to
 21 vertical Fe fluxes is at least an order lower than the vertical mixing fluxes. This might be
 22 underestimating the eddy effects in two ways. First, eddy activity is likely under-represented by
 23 the model in areas with relatively coarse resolution ($>5 \text{ km}$) due to the short Rossby radius (~ 15

km) in the Southern Ocean (Chelton et al. 1998). Secondly, Fe inputs due to upwelling and entrainment by mesoscale eddies can provide much needed Fe in areas with low surface Fe such as ACC frontal zones, particularly during the summer months.

4. Conclusions

A four-year (2003-2006) simulation has been conducted with a coupled physical-biogeochemical model (SOFe) for the Antarctic Peninsula, Drake Passage, Scotia Sea, and northern Weddell Sea. The model results have been validated with a suite of data from *in situ* observations and remote sensing, using quantitative metrics including RMSE, mean difference, and point-to-point correlation. All of these indicate a broad agreement between the model and observational data, including horizontal distributions and vertical structure of major currents and frontal positions (ACC, Antarctic Slope Front, Weddell Front), vertical mixing rate, and key water properties (T, S, Fe, nutrients, chlorophyll) within the model domain. In particular, modeled Fe concentrations agree reasonably well with measured concentrations obtained from two cruises conducted on the AP shelf and in the southern Drake Passage. A comparison of trajectories between modeled particles and drifters provides further evidence that the model successfully simulates the key features of the regional circulation, both on the shelf and in the open ocean. Significant model biases still exist including the unrealistically strong Sub-Antarctic Front. Modeling of vertical mixing also has rooms to improvement. In future work, explicit inclusion of tides in the model will likely remedy the simulation of near-bottom mixing to some degree.

We used the model to investigate the sources and transport pathways of dissolved Fe from the AP shelf toward the southern Scotia Sea, mainly using Fe distributions, currents, and

particle trajectories. The results indicate a complex transport pattern due to the convoluted shelf and open-ocean circulations in the region, both of which are largely guided by topographic constraints. The shallow and intricate corridor on the northwestern AP shelf from Adelaide Island to the SSIs is likely the dominant Fe source area, consistent with previous studies. Overall, Fe transport on the AP shelf converges from the western AP toward Elephant Island, with the Gerlache and Bransfield Strait Current system being the major conduit. The model results, however, also suggest that a significant amount of shelf-derived Fe is entrained by the SBdy over the northern slope of the SSIs through the Shackleton Fracture Gap toward the Ona Basin. Along the northern flank of Hesperides Trough, between Elephant Island and the South Orkney Islands, the SBdy further interacts with shelf currents to drive strong off-shelf export of dissolved Fe that originates from the AP shelf and local sediments, with additional contributions from the spillovers of Weddell waters. Once in the open ocean, shelf-derived Fe is advected downstream over the southern and eastern Scotia Sea, mainly via the SACCF, the SBdy and the Weddell Front. The model also indicates that a small amount of the shelf-derived Fe is advected further north by the SACCF toward the Polar Frontal Zone. Overall, however, waters with high dissolved Fe concentration are largely confined to the region south of the SACCF.

A budget estimate suggests that shelf-derived Fe is the dominant source of dissolved Fe in the southern Scotia Sea, meeting almost all of the Fe demand by the phytoplankton photosynthesis and accounting for >50% of the total Fe input to the euphotic zone (upper 100 m), with addition inputs from background Fe transported by the ACC and Weddell Gyre, dust deposition, deep-ocean sediment, and icebergs. The total off-shelf Fe export (within the top 500 m) from the South Scotia Ridge including the AP, Hesperides Trough, and SOP shelves is estimated to be 7.72×10^5 mol/day. Of this total transport, 5.25×10^5 mol/day (68%) derives purely

1 from the shelf sediment. About 70% of the off-shelf Fe transport, however, takes place below the
2 surface mixed layer, and is then re-supplied to the surface by vertical mixing.

3 **Acknowledgements:** MJ is funded by NOAA NA09OAR4310062, NSF ANT 0948378,
4 and HBOIF startup fund. STG received support from NSF awards ANT-0948338, PLR-1425989,
5 and OCE 1658001.

7 **References**

- 8
9 Anderson, T.R. and P. J. B. Williams, 1999, A one-dimensional model of dissolved organic
10 carbon cycling in the water column incorporating combined biological-photochemical
11 decomposition, *Global Biogeochem. Cycles*, 13(2), 337-349.
- 12 Andersson, A., K. Fennig, C. Klepp, S. Bakan, H. Gral, and J. Schulz, 2010, The Hamburg
13 Ocean Atmosphere Parameters and Fluxes from Satellite Data – HOAPS-3, *Earth Syst. Sci.*
14 *Data Discuss.*, **3**, 143-194, doi:10.5194/essdd-3-143-2010.
- 15 Annett, A.L., Skiba, M., Henley, S.F., Venables, H.J., Meredith, M.P., Statham, P.J., Ganeshram,
16 R.S., 2015. Comparative roles of upwelling and glacial iron sources in Ryder Bay, coastal
17 western Antarctic Peninsula. *Mar. Chem.* 176, 21–33.
18 <http://dx.doi.org/10.1016/j.marchem.2015.06.017>.
- 19 Annett, A.L., J. N. Fitzsimmons, M. J.M. Séguret, M. Lagerström, M. P. Meredith, O. Schofield,
20 R. M. Sherrell, 2017, Controls on dissolved and particulate iron distributions in surface
21 waters of the Western Antarctic Peninsula shelf, *Marine Chemistry*. 196: 81-97.
- 22 Antonov, J. I., D. Seidov, T. P. Boyer, R. A. Locarnini, A. V. Mishonov, H. E. Garcia, O. K.
23 Baranova, M. M. Zweng, and D. R. Johnson, 2010. *World Ocean Atlas 2009, Volume 2:*

1 *Salinity*. S. Levitus, Ed. NOAA Atlas NESDIS 69, U.S. Government Printing Office,
2 Washington, D.C., 184 pp.

3 Ardelan, M. V., O. Holm-Hansen, C. D. Hewes, C. S. Reiss, N. S. Silva, H. Dulaiova, E.
4 Steinnes, and E. Sakshaug, 2010, Natural iron enrichment around the Antarctic Peninsula in
5 the Southern Ocean, *Biogeosciences*, 7(1), 11-25.

6 Arrigo, K.R., G.L. van Dijken, and S. Bushinsky, 2008, Primary production in the Southern
7 Ocean, 1997–2006, *J. Geophys. Res.*, 113, C08004, doi:10.1029/2007JC004551.

8 Barbeau, K.A., J. W. Moffet, D. Caron, P. L. Croot, and D. Erdner, 1996, Role of protozoan
9 grazing in relieving iron limitation of phytoplankton. *Nature* 380: 61-64.

10 Barbeau, K.A., E. Rue, K. Bruland, and A. Butler, 2001, Photochemical cycling of iron in the
11 surface ocean mediated by microbial iron(III)- binding ligands. *Nature*, 413, 409–413.

12 Boyd, P.W. and M.J. Ellwood, 2010, Biogeochemical cycle of iron in the world ocean, *Nature*
13 *Biogeoscience*, 3: 675-682.

14 Boyd, P.W., Arrigo, K.R., Stzepek, R., and van Dijken, G.L., 2012. Mapping phytoplankton iron
15 utilization: insights into Southern Ocean supply mechanisms. *J. Geophys. Res.*, 117,
16 <http://dx.doi.org/10.1029/2011JC007726>.

17 Bundy R.M., M. Jiang, M. Carter, and K. A. Barbeau, 2016, Iron binding ligands in the
18 Southern California Current System: mechanistic studies, *Frontiers in Marine Science*, doi:
19 10.3389/fmars.2016.00027.

20 Capella, J., R. Ross, L.B. Quetin, and E.E. Hofmann, 1992, A note on the thermal structure of
21 the upper ocean in the Bransfield Strait-South Shetland Islands region. *Deep-Sea Research I*,
22 39 (7–8), 1221–1229.

Chelton, D.B. et al. 1998, Geographical Variability of the First Baroclinic Rossby Radius of Deformation, *J. Phy. Oceanogr.* 28: 433-460.

Collins, W. D., C. M. Bitz, M. L. Blackmon, G. B. Bonan, C. S. Bretherton, J. A. Carton, et al. 2006, The Community Climate System Model Version 3 (CCSM3), *Journal of Climate*, 19(11), 2122-2143.

Cunningham, S. A., S. G. Alderson, and B. A. King, M. A. Brandon, 2003, Transport and variability of the Antarctic Circumpolar Current in Drake Passage, *J. Geophys. Res.*, 108(C5), 8084, doi:10.1029/2001JC001147.

Dee, D. P., et al., 2011, The ERA-Interim reanalysis: Configuration and performance of the data assimilation system, *Q. J. R. Meteorol. Soc.*, 137, 553–597, doi:10.1002/qj.828.

Dong, S., Sprintall, J., Gille, S.T., Talley, L., 2008. Southern Ocean mixed-layer depth from Argo float profiles. *J. Geophys. Res.* 113, c06013, <http://dx.doi.org/10.1029/2006JC004051>.

Dulaiova, H. et al. 2009, Shelf-derived iron inputs drive biological productivity in the southern Drake Passage. *Global Biogeochemical Cycle*. GB4014. Vol. 23.

Elrod, V. A., Berelson, W. M., Coale, K. H., and Johnson, K. S. 2004, The flux of iron from continental shelf sediments: A missing source of global budgets. *Geophys. Res. Lett.*, 31, L12307, doi:10.1029/2004GL020216.

Fach B.A., Hofmann E.E., Murphy E.J., 2006, Transport of Antarctic krill (*Euphausia superba*) across the Scotia Sea. Part II: Krill growth and survival. *Deep-Sea Res I* 53: 1011–1043.

Fitzsimmons, J. N., E.A. Boyle, and W. J. Jenkins, 2014, Distal transport of dissolved hydrothermal iron in the deep South Pacific Ocean, *Proceedings of the National Academy of Sciences* 111, 16654-16661.

1 Fitzsimmons, J. N., S.G. John, C.M. Marsay, C.L. Hoffman, S.L. Nicholas, B.M. Toner, C.R.
2 German, R.M. Sherrell, 2017, Iron persistence in a distal hydrothermal plume supported by
3 dissolved-particulate exchange, *nature geoscience* 10, 195-203. DOI: 10.1038/NGEO2900.

4 Frants, M., S. T. Gille, M. Hatta, W. T. Hiscock, M. Kahru, C. I. Measures, B. G. Mitchell, and
5 M. Zhou, 2013a. Analysis of horizontal and vertical processes contributing to natural iron
6 supply in the mixed layer in southern Drake Passage, *Deep-Sea Res. II*, **90**, 68-76.

7 Frants, M., S. T. Gille, C. D. Hewes, O. Holm-Hansen, M. Kahru, A. Lombrozo, C. I. Measures,
8 B. G. Mitchell, H. Wang, and M. Zhou, 2013b. Optimal multiparameter analysis of source
9 water distributions in the southern Drake Passage, *Deep-Sea Res. II*, **90**, 31-42.

10 Gledhill, M., and K.N. Buck. 2012, The organic complexation of iron in the marine environment:
11 A review. *Frontiers in Microbiological Chemistry* 3: Article 69.

12 Gordon, A.L., Nowlin Jr., W.D., 1978. The basin waters of the Bransfield Strait. *Journal of*
13 *Physical Oceanography* 8, 258–264.

14 Hatta, M. Measures, C.I., Selph, K.E., Zhou, M., Yang, J.J., Hiscock, W.T., 2013, Iron fluxes
15 from the shelf regions near the South Shetland Islands in the Drake Passage during the
16 austral-winter 2006. *Deep-SeaRes. II* 90, 89–101.

17 Heywood, K.J., J. L. Collins, C. W. Hughes, I. Vassie, 2007, On the detectability of internal tides
18 in Drake Passage, *Deep-Sea Research I*, 54: 1972–1984.

19 Heywood, K.J., A.C. Naveira Garabato, D. P. Stevens, and R. Muench, 2004, On the fate of the
20 Antarctic Slope Front and the origin of the Weddell Front, *J. Geophys. Res.* 109, C06021.

21 Hopkinson, B. M., et al., 2007, Iron limitation across chlorophyll gradients in the southern Drake
22 Passage: Phytoplankton responses to iron addition and photosynthetic indicators of iron
23 stress. *Limnol. Oceanogr.* **52**: 2540-2554.

1 Hopkinson, B.M., Seegers, B., Hatta, M., Measures, C.I., Mitchell, B.G., Barbeau, K.A., 2013.
2 Planktonic C:Fe ratios and carrying capacity in the southern Drake Passage. *Deep-Sea Res.*
3 II 90, 102–111.

4 Hoppe, C.J.M., C. Klaas, S. Ossebaar, M. A. Soppa, W. Cheah, L. M. Laglera, J. Santos-
5 Echeandia, B. Rost, D. A. Wolf-Gladrow, A. Bracher, M. Hoppema, V. Strass, S.
6 Trimborn, 2017, Controls of primary production in two phytoplankton blooms in the
7 Antarctic Circumpolar Current, *Deep-Sea Research II*, 138: 63–73.

8 Hunke, E. C., 2001: Viscous-plastic sea ice dynamics with the EVP model: linearization issues, *J.*
9 *Comp. Phys.*, 170, 18-38.

10 Hunke, E. C. and J. K. Dukowicz, 1997: An elastic-viscous-plastic model for sea ice dynamics, *J.*
11 *Phys. Oceanogr.*, **27**, 1849-1868.

12 Jiang, M.S., K.A. Barbeau, F. Azam, K. Buck, C. I. Measures, G. Mitchell, K. Selph, and M.
13 Zhou, 2013a, The role of Fe ligands in controlling Fe cycle and phytoplankton productivity
14 in the Antarctic Peninsula, *Deep-Sea Research II*, 10.1016/j.dsr2.2013.01.029.

15 Jiang, M.S., M.A. Charette, C.I. Measures, Yiwu Zhu, and M. Zhou, 2013b, Seasonal cycle of
16 circulation in the Antarctic Peninsula and the off-shelf transport of shelf waters into Southern
17 Drake Passage and Scotia Sea, *Deep-Sea Research II*, DOI.10.1016/j.dsr2.2013.02.029.

18 Jiang, M., M. Kahru, C.I. Measures, K.E. Selph, and M. Zhou, 2018, Control of phytoplankton
19 blooms and variability in the Antarctic Peninsula, Drake Passage, southern Scotia Sea and
20 northern Weddell Sea, ms in prep.

21 Kahru, M., et al., 2007, Eddies enhance biological production in the Weddell-Scotia confluence
22 of the Southern Ocean. *Geophys. Res. Lett.*, 34 (14): L14603. DOI: 10.1029/2007GL030430.

23 Kim, Y. and A. H. Orsi, 2014, On the variability of Antarctic Circumpolar Current Fronts

inferred from 1992–2011 altimetry, *J. Phys. Oceanogr.* 44, 3054-3071.

Korb, R.E., Whitehouse, M.J., Ward, P., Gordon, M., Venables, H.J., and Poulton, A.J. 2012, Regional and seasonal differences in microplankton biomass, productivity, and structure across the Scotia Sea: Implications for the export of biogenic carbon, *Deep-Sea Research II*, 59-60, 67-77.

Lancelot, C., A. de Montety, H. Goosse, S. Becquevort, V. Schoemann, B. Pasquer, and M. Vancoppenolle, 2009, Spatial distribution of the iron supply to phytoplankton in the Southern Ocean: A model study, *Biogeosciences*, 6, 2861–2878, doi:10.5194/bg-6-2861-2009.

Lannuzel, D., Schoemann, V., de Jong, J., Chou, L., Delille, B., Becquevort, S., Tison, J.L., 2008. 2008. Iron study during a time series in the western Weddell pack ice. *Mar. Chem.* 108, 85–95.

Large, W.G., McWilliams, J.C., Doney, S.C., 1994. Oceanic vertical mixing: a review and a model with a nonlocal boundary layer parameterization. *Reviews of Geophysics* 32 (4), 363–403.

Lin, H., Rauschenberg, S., Hexel, C.R., Shaw, T.J., and Twining, B .S., 2011. Free-drifting icebergs as sources of iron to the Weddell Sea. *Deep Sea Res. Part II.*, 1392–1406, <http://dx.doi.org/10.1016/j.dsr2.2010.11.020>.

Locarnini, R. A., A. V. Mishonov, J. I. Antonov, T. P. Boyer, H. E. Garcia, O. K. Baranova, M. M. Zweng, and D. R. Johnson, 2010. *World Ocean Atlas 2009, Volume 1: Temperature*. S. Levitus, Ed. NOAA Atlas NESDIS 68, U.S. Government Printing Office, Washington, D.C., 184 pp.

1 Luo, C., Mahowald, N. M., Meskidze, N., Chen, Y., Siefert, R. L., Baker, A. R., and Johansen,
2 A. M. 2005, Estimation of iron solubility from observations and a global aerosol model, J.
3 Geophys. Res., 110, D23307, doi:10.1029/2005D006059.

4 Mahowald, N. M., et al. 2005, Atmospheric global dust cycle and iron inputs to the ocean,
5 Global Biogeochem. Cy., 19, Gb4025, doi:10.1029/2004gb002402, 2005.

6 Martin, J.H., R.M. Gordon, and S.E. Fitzwater, 1990, Iron in Antarctic waters. Nature, 345, 156-
7 158.

8 Measures, C.I., Hatta, M., Grand, M.M., 2012, Bioactive trace metal distributions and
9 biogeochemical controls in the Southern Ocean. *Oceanography*, 25, 122-133.

10 Measures, C.I., Brown, M.T., Selph, K.E., Apprill, A., Zhou, M., Hatta, M., Hiscock, W.T., 2013.
11 The influence of shelf processes in delivering dissolved iron to the HNLC waters of the
12 Drake Passage, Antarctica. *Deep-Sea Res. II* 90, 77–88.

13 Mellor, G. L. and L. Kantha, 1989, An ice-ocean coupled model, *J. Geophys. Res.*, **94**, 10,937-
14 10,954.

15 Mitchell, B.G., Brody, E.A., Holm-Hansen, O., McClain, C., Bishop, J., 1991. Light limitation of
16 phytoplankton biomass and macronutrient utilization in the Southern Ocean. *Limnology and*
17 *Oceanography* 36, 1662–1677.

18 Moore, J.K. and O. Braucher, 2008, Sedimentary and mineral dust sources of dissolved iron to
19 the world Ocean. *Biogeosciences*, 5: 631–656.

20 Naveira Garabato, A.C., Polzin, K.L., King, B.A., Heywood, K.J., Visbeck, M., 2004.
21 Widespread intense turbulent mixing in the Southern Ocean. *Science* 303 (5655), 210–213.

1 Nelson, DM and W.O. Smith, 1991, Sverdrup revisited – critical depths, maximum chlorophyll
2 levels, and the control of Southern Ocean productivity by the irradiance-mixing regime,
3 Limnol. and Oceanogr., 36(8): 1650-1661.

4 Nielsdóttir, M.C., et al., 2011. Seasonal and spatial dynamics of iron availability in the Scotia
5 Sea. Mar. Chem. 130–131, 62–72.

6 Okubo, A., 1971, Oceanic diffusion diagrams, Deep-Sea Research, 1971, 18, 789-802.

7 Orsi, A. H., T. Whitworth, and W.D. Nowlin, 1995, On the meridional extent and fronts of the
8 Antarctic circumpolar current. Deep-Sea Res. I. 42: 641-673.

9 Padman, L., S. L. Howard, and R. D. Muench, 2006, Internal tide generation along the South
10 Scotia Ridge, Deep Sea Res., Part II, 53, 157–171.

11 Parekh, P., M. Follows, and E. Boyle, 2004, Modelling the global ocean iron cycle, Global
12 Biogeochem. Cycle, 18, GB1002, doi:10.29/2003GB002061.

13 Piñones A., Hofmann E. E., Daly K.L., Dinniman M. S., Klinck, J. M. 2013a. Modeling the
14 remote and local connectivity of Antarctic krill populations along the western Antarctic
15 Peninsula. Mar. Ecol. Prog. Ser. 481: 69–92

16 Piñones A., Hofmann E. E., Daly K.L., Dinniman M.S., Klinck, J. M., 2013b, Modeling
17 environmental controls on the transport and fate of early life stages of Antarctic krill
18 (*Euphausia superba*) on the western Antarctic Peninsula continental shelf, Deep-Sea
19 Research I, 82, 17–31.

20 Platt, T., et al., 1980, Photoinhibition of photosynthesis in natural assemblages of marine
21 phytoplankton, *J. Mar. Res.*, **38**, 687-701.

22 Reiss, S and M. Jiang, 2018, The connectivity and retention of Antarctic krill in the northern
23 Antarctic Peninsula, ms in prep.

1 Russell, J.L. et al. 2006, The Southern Hemisphere westerlies in a warming world: Propping
2 open the door to the deep ocean, *J. Climate*, 19: 6382-7390.

3 Sañudo-Wilhelmy, S.A., Olsen, K.A., Scelfo, J.M., Foster, T.D., Flegal, A.R., 2002. Trace metal
4 distributions off the Antarctic Peninsula in the Weddell Sea. *Marine Chemistry*, 77,157–170.

5 Sato, M., S. Takeda, and K. Furuya. 2007. Iron regeneration and organic iron(III)-binding ligand
6 production during *in situ* zooplankton grazing experiment. *Marine Chemistry* 106: 471-488.

7 Shchepetkin, A.F., and J.C. McWilliams, 2003, A method for computing horizontal pressure-
8 gradient force in an oceanic model with a non-aligned vertical coordinate. *J. Geophys. Res.*
9 108 (C3), 3090.

10 Shchepetkin, A.F. and J. C. McWilliams, 2005, The regional oceanic modeling system (ROMS):
11 a split-explicit, free-surface, topography-following-coordinate oceanic model. *Ocean*
12 *Modelling*, 9: 347–404.

13 Schlitzer, R. and the GEOTRACES Group, 2018, The GEOTRACES Intermediate Data Product
14 2017. *Chemical Geology*. 493. 210-223. doi:10.1016/j.chemgeo.2018.05.040.

15 Smagorinsky, J., 1963, General circulation experiments with the primitive equations, *Mon.*
16 *Weather Rev.*, 91: 99–164.

17 Song, Y. and D. B. Haidvogel, 1994: A semi-implicit ocean circulation model using a
18 generalized topography-following coordinate system, *J. Comp. Phys.*, **115** (1), 228-244.

19 Tagliabue, A., J.-B. Sallée, A. R. Bowie, M. Lévy, S. Swart and Philip W. Boyd, 2014, Surface-
20 water iron supplies in the Southern Ocean sustained by deep winter mixing, *Nature*
21 *Geosciences*, DOI: 10.1038/NGEO2101.

22 Thompson, A.F., and K. J. Heywood, 2008, Frontal structure and transport in the northwestern
23 Weddell Sea, *Deep-Sea Research I* 55, 1229– 1251.

1 Thompson, A.F., K. J. Heywood, S.E. Thorpe, A.H.H. Renner, and A. Trasvina, 2009, Surface
2 Circulation at the Tip of the Antarctic Peninsula from Drifters, J. Phys. Oceanogr., 39, 3-26.

3 Thompson, A.P. and M. Youngs, 2013, Surface exchange between the Weddell and Scotia Seas,
4 Geophys. Res. Lett. 40, 1–6, doi:10.1002/2013GL058114

5 Thorpe S.E, Murphy E.J., Watkins J.L. 2007, Circumpolar connections between Antarctic krill
6 (*Euphausia superba* Dana) populations: investigating the roles of ocean and sea ice transport.
7 Deep-Sea Res I 54:792–810

8 Trick, C.G., 1989. Hydroxamate-siderophore production and utilization by marine eubacteria.
9 Current Microbiology 18, 375-378.

10 von Gyldenfeldt, A. B., E. Fahrbach, M. A. Garcia, and M. Schroder, 2002, Flow variability at
11 the tip of the Antarctic Peninsula, Deep Sea Res., Part II, 49, 4743– 4766.

12 Venables, H., and Moore, C.M., 2010. Phytoplankton and light limitation in the Southern Ocean:
13 learning from high-nutrient, high-chlorophyll areas. Journal of Geophysical Research –
14 Oceans, 115, Art. No. C02015Feb27.

15 Wadley M.R., T. D. Jickells, and K. J. Heywood, 2014, The role of iron sources and transport for
16 Southern Ocean productivity, Deep-Sea Research I 87(2014)82–94.

17 Webb, D.J., B. A. de Cuevas and A. C. Coward, 1998, The first main run of the OCCAM global
18 ocean model, Southampton Oceanography Centre, Internal Document No. 34.

19 Youngs, M.K. et al., 2015, Weddell Sea export pathways from surface drifters, J. Phys.
20 Oceanogr., 45: 1,068.

21 Zhou, M., Niiler, P.P., Hu, J.-H., 2002. Surface current in the Bransfield and Gerlache Straits
22 measured by surface Lagrangian drifters. Deep-Sea Research I 46, 267–280.

- 1 Zhou, M., Pearn, P., Zhu, Y., Dorland, R., 2006, The western boundary current in the Bransfield
2 Strait, Antarctica, Deep-Sea Res. I, 53: 1244-1252.
- 3 Zhou, M., Y. Zhu, and R.D. Dorland, 2010, Dynamics of the current system in the southern
4 Drake Passage. Deep-Sea Res. I, 57: 1039-1048.
- 5 Zhou, M. Zhu, Y., Measures, C.I., Hatta, M., Selph, K.E., Charette, M., Gille, S., Frants, M.,
6 Jiang, M., Mitchell, B.G., 2013, Winter mesoscale circulation on the shelf slope region of the
7 southern Drake Passage. Deep-Sea Research II, 90, 4–14.
- 8
- 9

Captions

Table 1. Modifications of model parameters from 1-D simulation (Jiang et al., 2013a).

Table 2. Quantitative metrics for the model skills.

Table 3. Multiyear (2003-2006) mean upper 500 m off-shelf Fe flux (10^4 mol/day).

Table 4. An Fe budget for the euphotic zone (0 – 100 m) of the southern Scotia Sea.

Figure 1. Model grid (sub-sampled 1 per 3 grid lines) and topography for the study area.

Acronyms: BB – Burdwood Bank, STR – Shackleton Traverse Ridge, TR – Terror Rise,

PB – Pirie Bank, BrB – Bruce Bank, DB – Discovery Bank, SSIs – South Shetland

Islands, EI – Elephant Island, CI – Clarence Island, BS – Bransfield Strait, HT –

Hesperides Trough, PoB – Powell Basin, GS – Gerlache Strait, AS – Antarctic Sound, JR

– Joinville Ridge.

Figure 2. A diagram for the biogeochemical model (SOFe) (reproduced from Jiang et al. 2013a).

Color codes are for nitrogen (black), silica (red), and Fe (green) flows, respectively. For

clarity some minor elemental flows were not included. No sediment sub-model is

incorporated in the current study. Bio-available Fe includes both dissolved inorganic Fe

and Fe bound to organic ligands.

Figure 3. (a) Sediment Fe flux (mol/sec) in this study (red) and that used by Wadley et al. (2014)

(blue), and (b) Fe concentration (nM) versus Si(OH)_4 concentration (μM) at two stations

representing the ACC waters during the summer (LGM0402) cruise. The blue line

represents the best exponential fit, $y = 0.0701e^{0.0194x}$ ($r=0.88$, $p<0.01$).

Figure 4. Monthly mean sea level from AVISO (a) and model (c) during August 2006, and (c)

multityear mean and standard deviation (STD) of SSH along a transect (black line in (b))

from Weddell Sea to Drake Passage. No valid satellite altimetry data exists in Weddell

Sea and much of the AP shelf (blank area) during winter time. White lines indicate the ACC fronts (Orsi et al. 1995).

Figure 5. Trajectories of surface drifters (a) (data source: <https://gdp.aoml.gov/>) and model neutrally buoyant particles (b) released from the AP shelf. Modeled particles were uniformly seeded over the AP waters (inside the black box with dots indicating the initial positions) and continuously released for 2 months starting June 1, 2006. White dashed and solid lines indicate the ACC fronts and SBdy, respectively.

Figure 6. Vertical mixing from estimates based on *in situ* measurements and model output for Drake Passage (a), north Scotia Ridge (b), south Scotia Ridge (c), and southern Scotia Sea (d). The *in situ* estimates were derived from Naveira Garabato et al. (2008). Model output is from summer (February) 2006.

Figure 7. Surface Fe concentrations from field measurement (a) and model (b), vertical mean profiles and standard deviation of Fe concentration (c), and the point-to-point correlation between model and measured Fe concentrations for the surface (d) and all depths (e) during the LMG0402 cruise (Feb-Mar. 2004).

Figure 8. (a-f) Modeled (a, c, e) and field measured Fe concentrations (b, d, f) during the NBP0606 cruise along the three transects across the Bransfield Strait. (g) The model transects (solid lines) and stations (dots) (blue line: a & b; red line: c & d; black line: e & f). (h) The vertical mean profiles and standard deviation. (i)-(j) the scatter plot of the point-to-point modeled versus data for (i) the surface only and (j) data from all depths (solid lines are the best linear regression between model-data).

Figure 9. Monthly means of model surface chlorophyll (a, c, e) and the monthly composites of MODIS surface chlorophyll (b, d, f) for October 2005 (a, b), January 2006 (c, d) and April 2006 (e, f), respectively.

Figure 10. Horizontal distributions of modeled surface dissolved Fe in August 2006. The black lines indicate the two N-S south transects: mid-Bransfield transect (across the Antarctic Sound and King George Island), and Weddell-Drake Passage (from Powell Basin to Ona Basin), respectively. The red dotted line indicates the along-shelf transect from Adelaide Island to Elephant Island, SOI and Discovery Bank (AI-EI-SOI-DB) for estimates of cross-shelf Fe transport shown in Figures 14 and 15. White lines indicate the ACC fronts (from north to south): SAF, PF, SACCF, and SBdy.

Figure 11. Vertical distributions of model dissolved Fe concentration during August 2006 along (a) the mid-Bransfield transect (across the Antarctic Sound and King George Island, shown in a black line in Figure 10) and (b) Weddell-Drake Passage transect (from Powell Basin to Ona Basin, shown in a black line in Figure 10).

Figure 12. Horizontal distributions of modeled dissolved Fe concentration (color) and currents (arrows) at 200 m in August 2006 for Elephant Island area (a) and around Terror Rise (b). White dashed and solid lines indicate the ACC fronts (PF and SACCF) and SBdy fronts, respectively. Red dotted line indicates the portions of along-shelf transect in Figure 10.

Figure 13. Trajectories of surface drifters (left panels) and modeled particles (right panels). The black box shows the released area: the northern SSIs shelf (a, b), the southern Bransfield Strait shelf (c, d), the northwest Weddell Sea (e, f) and the western Antarctic Peninsula shelf (g, h).

Figure 14. (a) Vertical distributions of (a) temperature ($^{\circ}\text{C}$), (b) cross-section velocity (m/sec) (northward positive), and (c) dissolved Fe concentration (nM) along the shelf edge transect (see red dotted line in Figure 10).

Figure 15. Depth-integrated off-shelf transport flux of dissolved Fe (mol/day) in the entire water column (a) and the upper 500 m (b) for total blue dots) and shelf-derived Fe only (red dots) along the AI-EI-SOI-DB transect. The flux is computed at 15 km increment.

Figure 16. Multi-year (2003-2006) average of vertical Fe flux ($\mu\text{mol}/\text{m}^2/\text{year}$) at the base of the mixed layer in summer (December-February) (a) and winter (June-August) (b). The base of the mixed layer is defined as 50 m for the summer and 100 m for the winter.

1 **Table 1. Modifications of model parameters from 1-D simulation (Jiang et al., 2013a)**

| Model parameters (unit) | 1-D model | This study |
|--|-----------|------------|
| Light attenuation due to seawater (1/m) | 0.033 | 0.025 |
| PAR fraction of shortwave radiation (dimensionless) | 0.43 | 0.5 |
| Phytoplankton self-shading (m^2/mmolN) | 0.02 | 0.04 |
| Maximum growth rate for small phytoplankton (1/day) | 1.6 | 2.0 |
| Phytoplankton mortality for both diatoms and small phytoplankton (1/day) | 0.05 | 0 |
| Small phytoplankton respiration rate (1/day) | 0.1 | 0.05 |
| Q10 for small phytoplankton (dimensionless) | 0.05 | 0.04 |
| Q10 for diatoms (dimensionless) | 0.05 | 0.06 |
| Small phytoplankton sinking velocity (m/day) | 0 | 0.05 |
| Diatoms sinking velocity (m/day) | 1 | 2 |
| Microzooplankton grazing rate (1/day) | 1.1 | 1.2 |
| Half saturation constant for microzooplankton grazing ($\mu\text{molN/l}$) | 0.1 | 0.2 |
| Half saturation constant for mesozooplankton grazing ($\mu\text{molN/l}$) | 0.3 | 0.5 |
| Microzooplankton mortality rate (1/day) | 0.05 | 0.15 |
| Mesozooplankton mortality rate (1/day) | 0.05 | 0.10 |
| Mesozooplankton assimilation efficiency (dimensionless) | 0.7 | 0.9 |
| Q10 for microzooplankton (dimensionless) | 0.81 | 0.71 |
| Q10 for mesozooplankton (dimensionless) | 0.81 | 0.71 |
| Microzooplankton feeding preference for bacteria (dimensionless) | 0.3 | 0.4 |
| Microzooplankton feeding preference for small phytoplankton (dimensionless) | 0.6 | 0.5 |
| Mesozooplankton feeding preference for diatoms (dimensionless) | 0.3 | 0.25 |
| Mesozooplankton feeding preference for microzooplankton (dimensionless) | 0.7 | 0.75 |
| Half saturation constant for small phytoplankton Fe uptake (nM) | 0.05 | 0.1 |
| Half saturation constant for diatoms Fe uptake (nM) | 0.1 | 0.2 |
| Dissolved Fe particle-dependent scavenging rate ($1/\mu\text{M/day}$) | 0.01 | 0.05 |
| Fe ligand productivity rate (1/day) | 12 | 3 |

2

Table 2. Statistics for model-data comparison

| Dataset | Parameter/Period/ Area | RMSE | Point-to- point correlation ¹ | Mean±STD | | Mean difference (confidence interval) ² |
|--|---------------------------|------|--|------------|------------|---|
| | | | | Model | Data | |
| LMG0402 (Feb-Mar, 2004) | Temperature (°C) | 0.54 | 0.84 | 1.30±0.91 | 1.16±1.0 | 0.14 (0.13-0.15) |
| | Salinity (psu) | 0.08 | 0.95 | 34.50±0.24 | 34.52±0.24 | 0.023 (0.022-0.024) |
| | NO ₃ (μM) | 2.8 | 0.69 | 29.2±3.9 | 28.7±3.3 | 0.5 (0.2-0.8) |
| | Si(OH) ₄ (μM) | 13.3 | 0.79 | 69.5±16.3 | 56.5±21.7 | 13 (11.5-14.5) |
| | Fe (nM) | 0.47 | 0.45 | 0.56±0.49 | 0.43±0.39 | 0.14(0.1-0.18) |
| | MLD (m) | 16.8 | 0.18 | 35.5±0.5 | 40.8±15.7 | 5.3 (2.0-8.6) |
| NBP0606 (Jul-Aug. 2006) | Temperature (°C) | 0.54 | 0.9 | 0.43±1.20 | 0.33±1.23 | 0.1 (0.09-0.11) |
| | Salinity (psu) | 0.1 | 0.88 | 34.51±0.21 | 34.52±0.20 | * |
| | Fe (nM) | 0.67 | 0.81 | 1.50±0.97 | 1.80±1.07 | 0.3 (0.25-0.35) |
| | MLD | 83.6 | 0.19 | 80.0±22.0 | 99.6±49.0 | 19.6 (4.5-34.5) |
| AVISO SSH | August 2006 | 0.16 | 0.95 | 0.58±0.46 | 0.60±0.49 | * |
| MODIS Chlorophyll | October 2005 | 0.56 | 0.27 | 0.59±0.28 | 0.42±0.64 | 0.17 (0.13-0.20) |
| | January 2006 | 0.79 | 0.36 | 0.80±1.3 | 0.55±0.62 | 0.25 (0.22-0.28) |
| | April 2006 | 0.24 | 0.65 | 0.59±0.12 | 0.64±0.53 | 0.05 (0.03-0.07) |
| Dong et al. (2008)³ | MLD (February) | 16.5 | 0.40 | 40.8±13.7 | 51.3±16.3 | 10.5 (9.6-12.4) |
| | MLD (August) | 78.9 | 0.55 | 125.9±50.7 | 155.8±94.7 | 29.9 (25.7-34.1) |
| BAS (Nov. 2006) | Temperature (°C) | 0.71 | 0.88 | 0.76±1.05 | 0.99±1.42 | 0.23 (0.07-0.39) |
| | Salinity (psu) | 0.11 | 0.96 | 34.26±0.26 | 34.23±0.33 | * |
| | Fe (nM) | 0.33 | 0.76 | 0.61±0.30 | 0.35±0.50 | 0.26 (0.18-0.34) |
| SOC Vertical Mixing⁴ | Drake Passage | 0.38 | 0.47 | -4.51±0.22 | -4.24±0.44 | 0.27 (0.24-0.30) |
| | North Scotia Ridge | 0.50 | 0.63 | -4.16±0.59 | -3.62±0.60 | 0.52 (0.46-0.58) |
| | South Scotia Ridge | 0.42 | 0.30 | -4.40±0.35 | -4.60±0.34 | 0.20 (0.14-0.24) |
| | Southern Scotia Sea | 0.34 | 0.84 | -4.20±0.55 | -3.99±0.57 | 0.16 (0.13-0.19) |

¹Bold values indicate significant correlation or mean difference at $p<0.05$.

²The mean difference (last column) was tested with the paired student- t test. *indicate insignificant difference.

³Model results are derived from 4-year (2003-2006) average.

⁴All computation was based on the logarithmically transformed vertical mixing $\mu=\log_{10}(k_v)$.

1
2
3
4
5
6
7
8

9
10

Table 3. Annual mean off-shelf Fe flux (10⁵ mol/day) in 2003-2006

| Segment | | AI-EI | EI-SOI | SOI-DB | Total |
|---------------------|---------------|-----------|-----------|-----------|-----------|
| 0-100 m | Total | 1.08±0.60 | 0.80±0.37 | 0.61±0.38 | 2.48±1.16 |
| | Shelf-derived | 0.88±0.52 | 0.57±0.32 | 0.23±0.23 | 1.68±0.9 |
| 0-500 m | Total | 2.59±1.08 | 2.69±0.90 | 2.44±0.56 | 7.72±1.26 |
| | Shelf-derived | 2.16±0.89 | 1.90±0.74 | 1.19±0.42 | 5.25±1.07 |
| Entire water column | Total | 2.45±1.07 | 4.73±1.64 | 4.76±0.93 | 11.9±2.0 |
| | Shelf-derived | 2.12±0.88 | 2.50±0.97 | 1.45±0.49 | 6.08±1.2 |

1
2
3
4
5
6
7
8
9
10
11
12
13
14
15

Table 4. Fe budget for the southern Scotia Sea (top 100 m)

| | Flux (10^5 mol/day) |
|--|------------------------|
| Phytoplankton Fe uptake ¹ | 2.56±2.61 |
| ACC transport | 0.055 |
| Cross-shelf transport (shelf-derived Fe) | 1.68±0.90 |
| Cross-shelf transport (background Fe) | 0.80±0.09 |
| Vertical mixing at 100 m | 0.84±1.20 |
| Dust deposition ² | 0.26 |
| Iceberg ² | 0.38 |
| Total Fe input | 4.00 |

¹A Fe/C ratio of 3×10^{-5} mol/mol is used in the model. The area mean new productivity is 124.5 ± 127.1 mgC/m²/day for an area 8.25×10^{11} m².

²Assuming dust deposition and icebergs each supplies 10% and 15% of the productivity demand (Wadley et al. 2014).

16
17
18
19
20
21

1 Figure 1

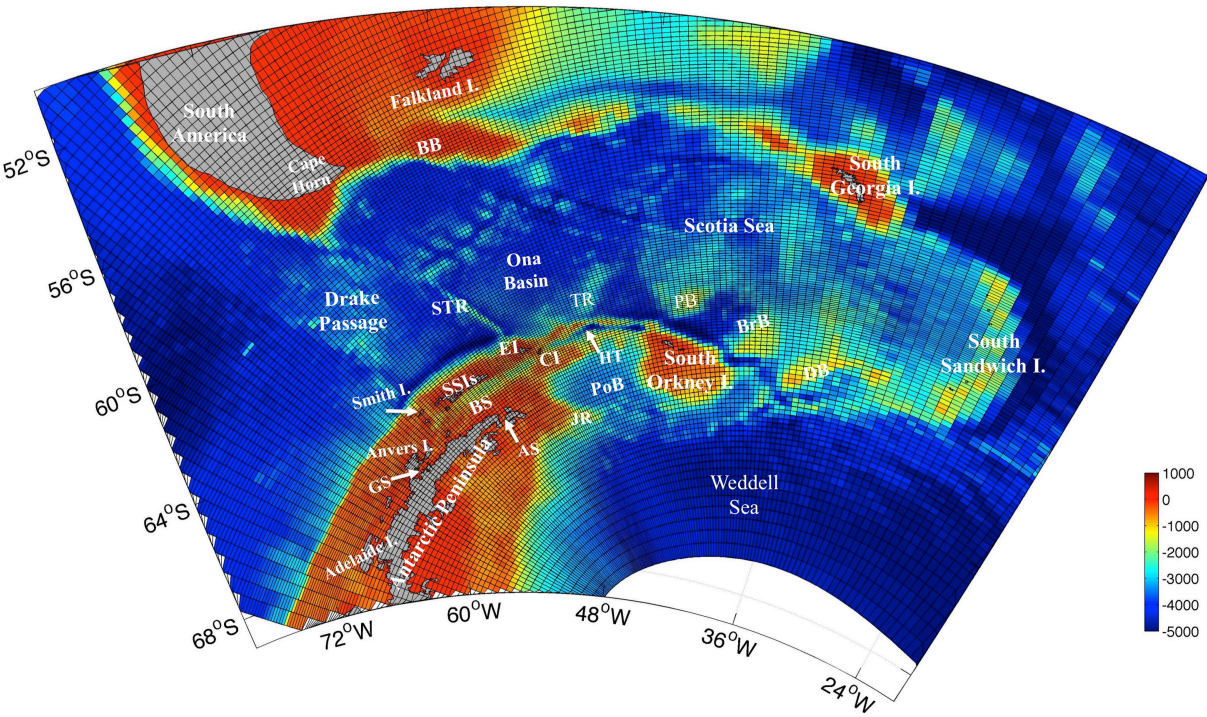
2

3

4

5

6



7

8

9

Figure 2

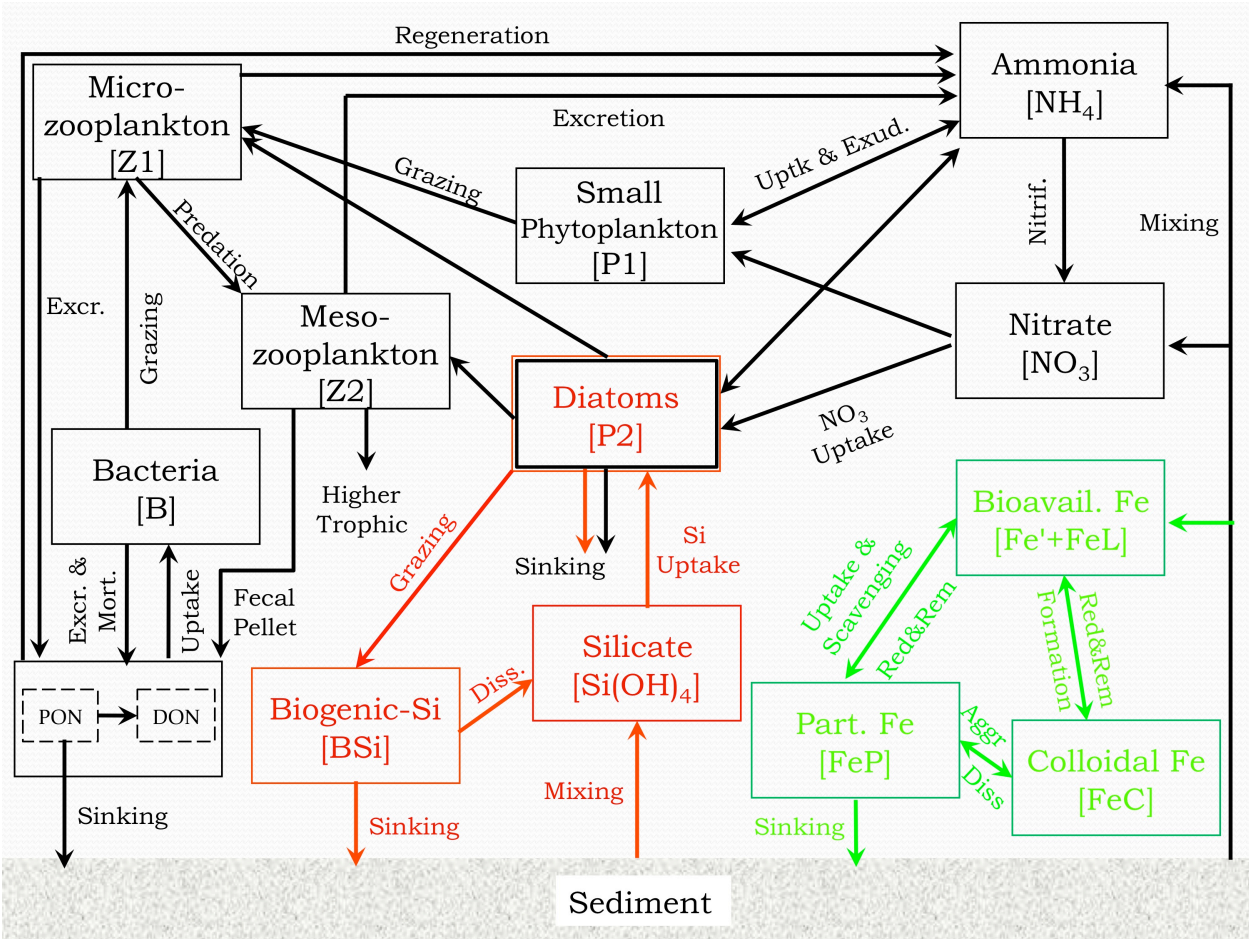
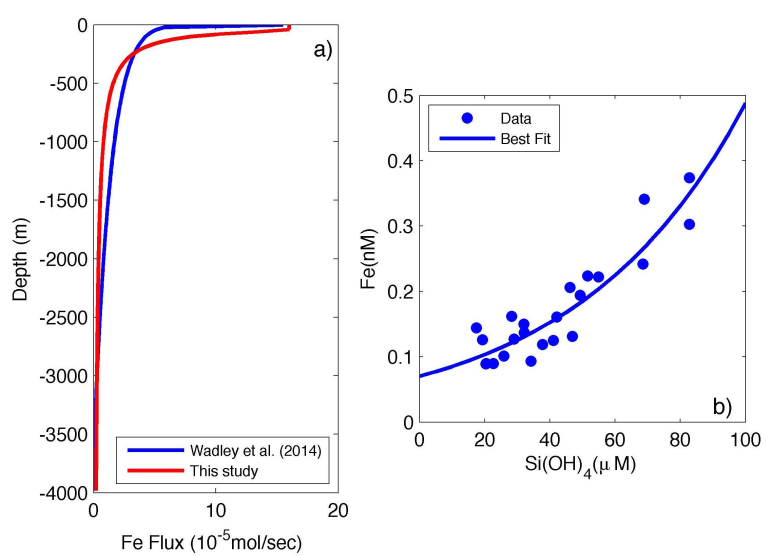
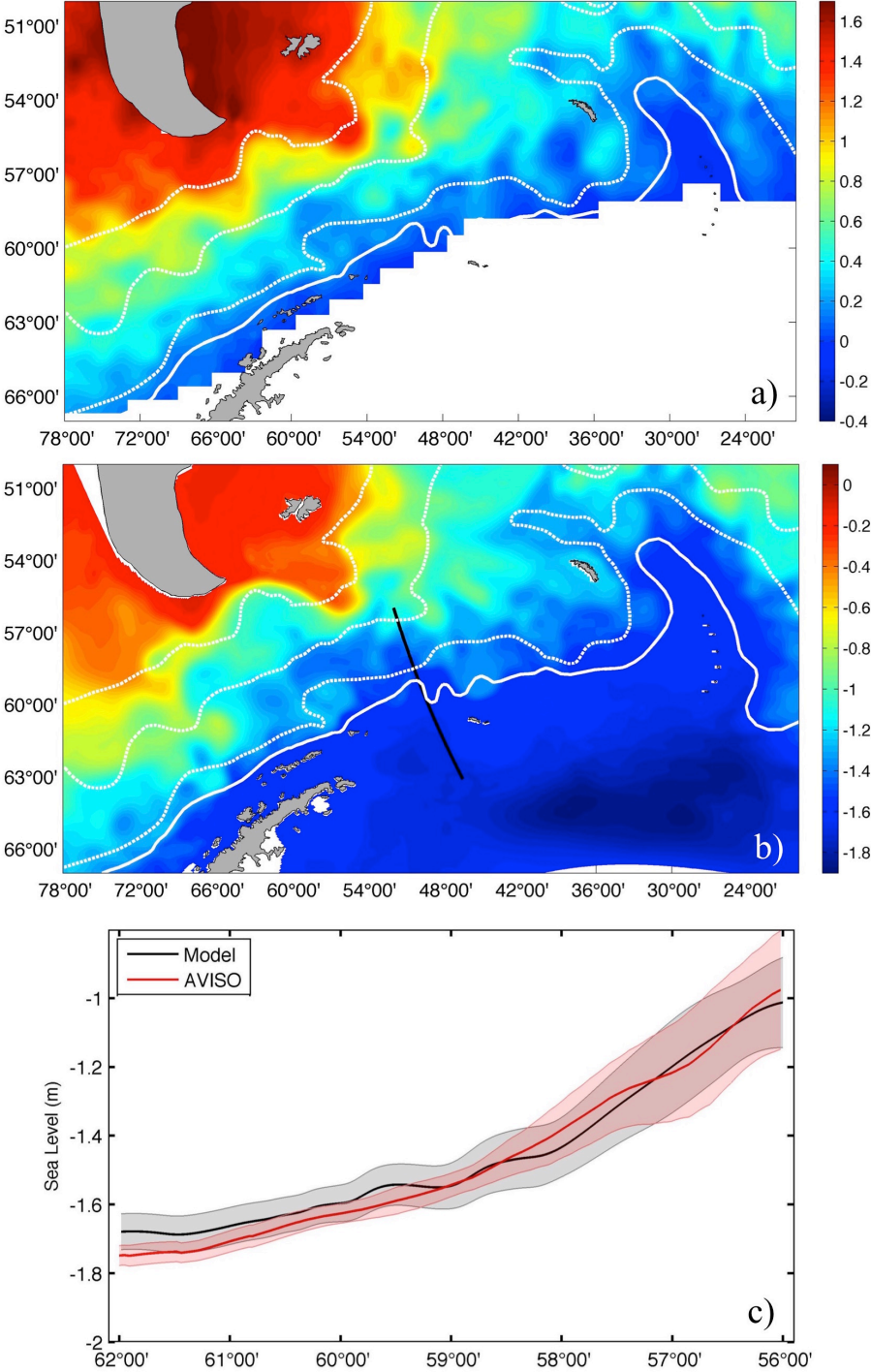


Figure 3.



1 Figure 4.

2
3

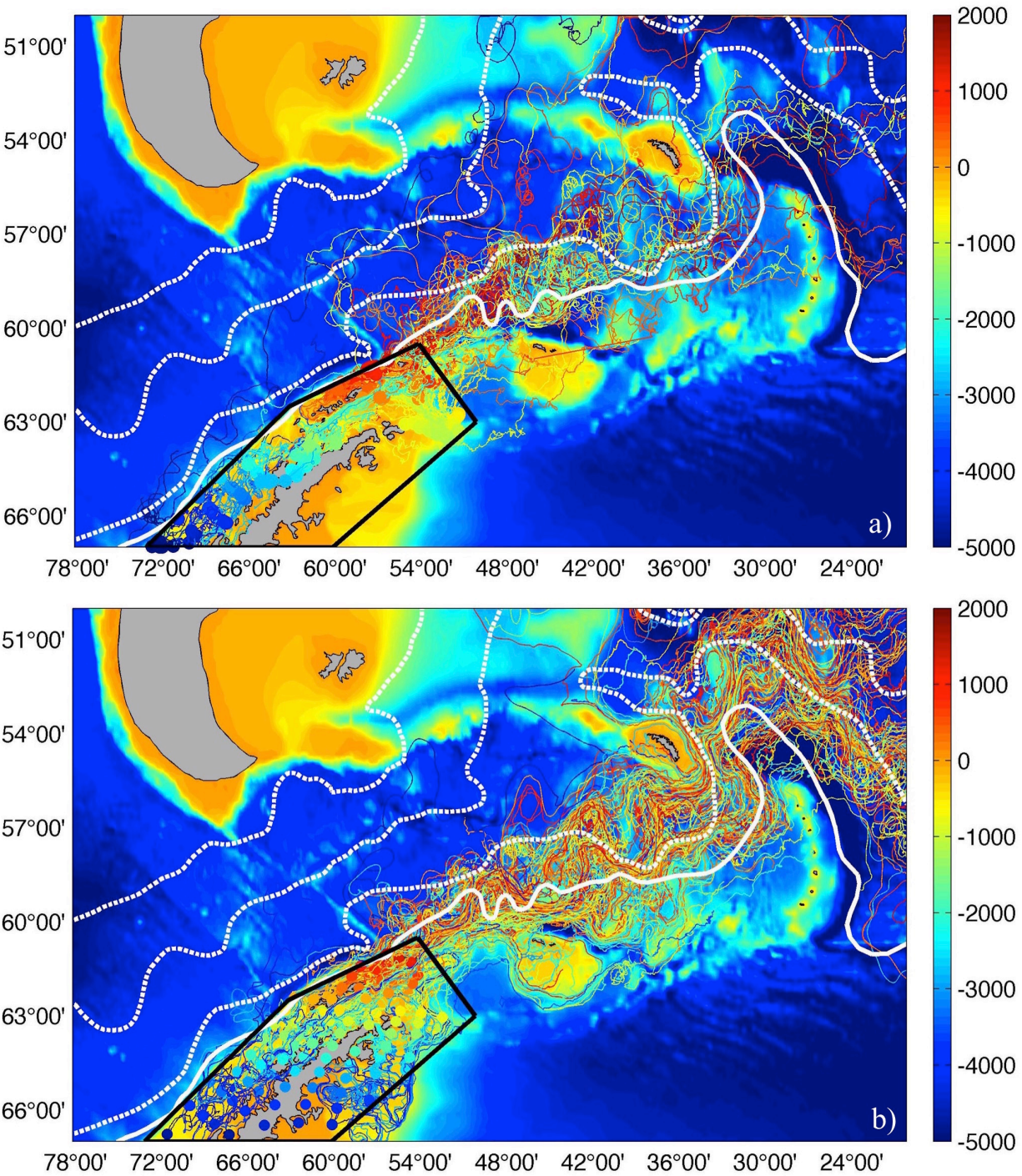


4
5
6

1 Figure 5.

2

3



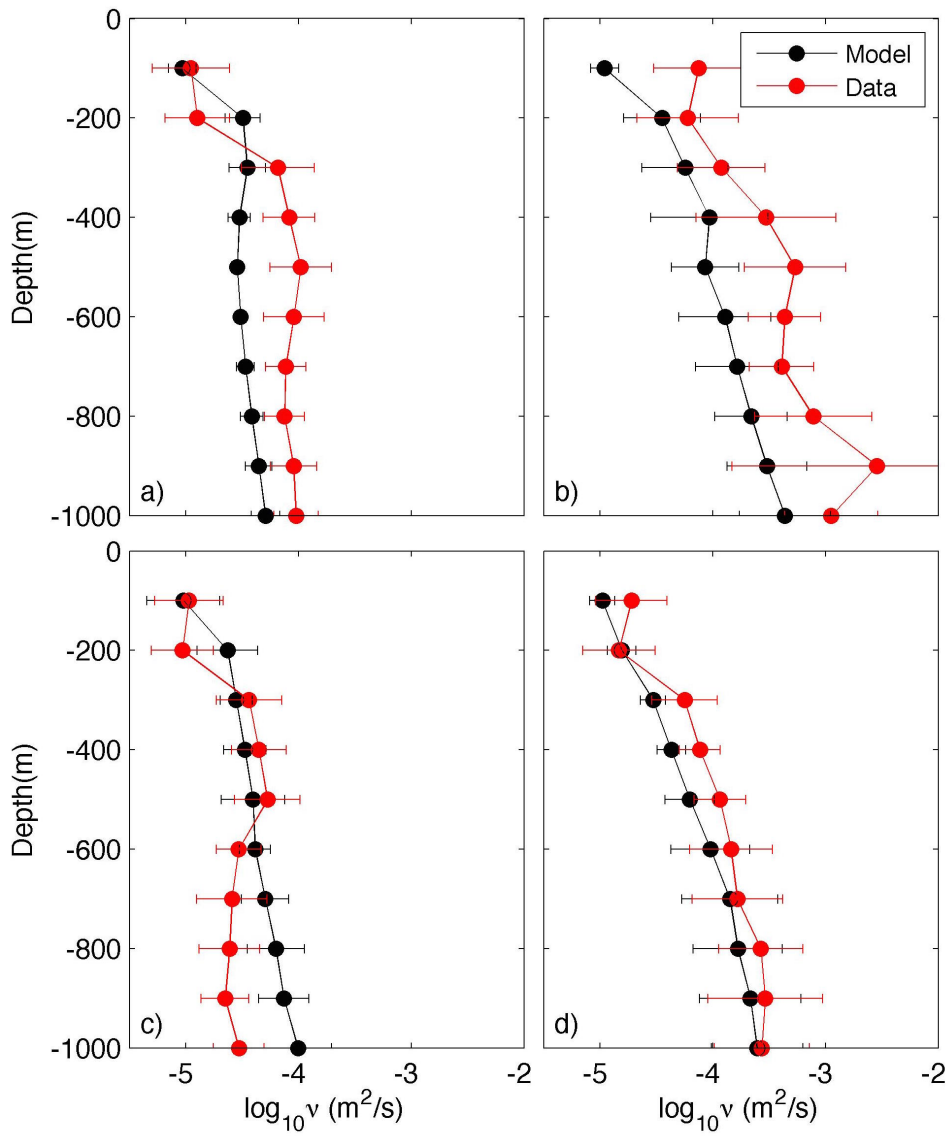
4
5

1 Figure 6.

2

3

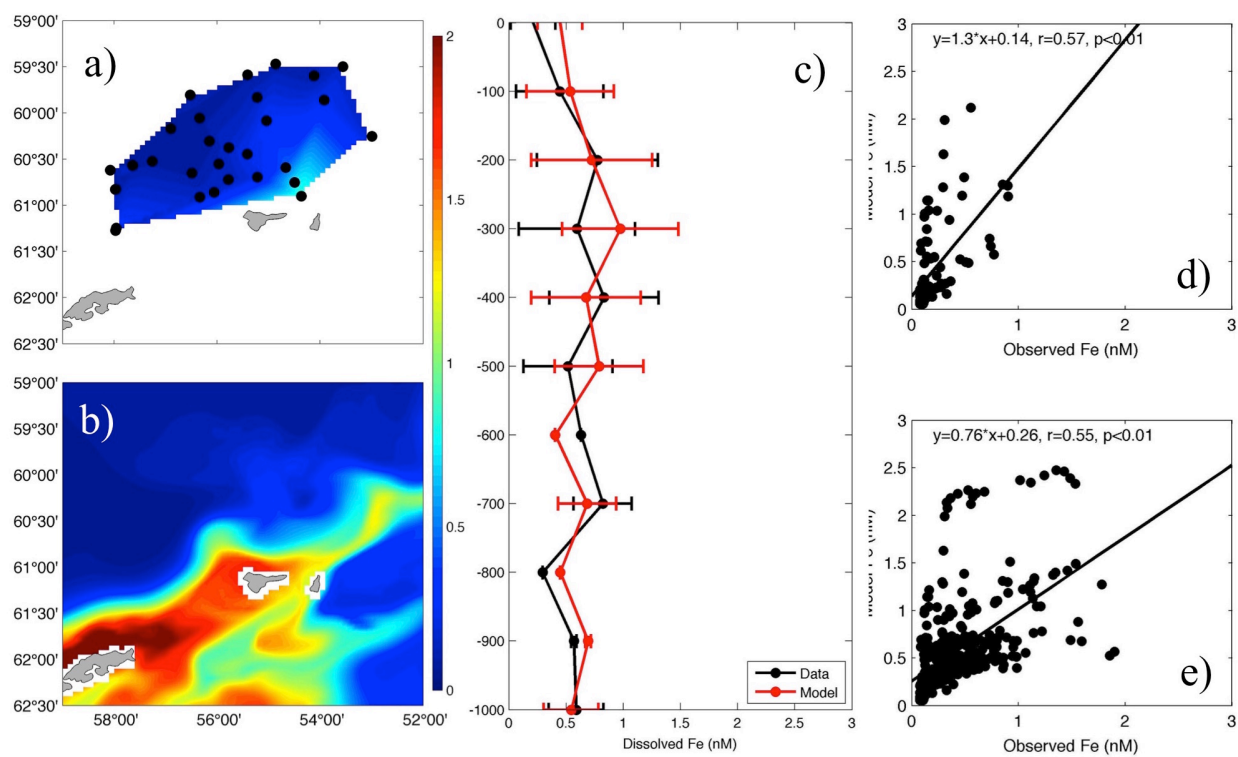
4



5

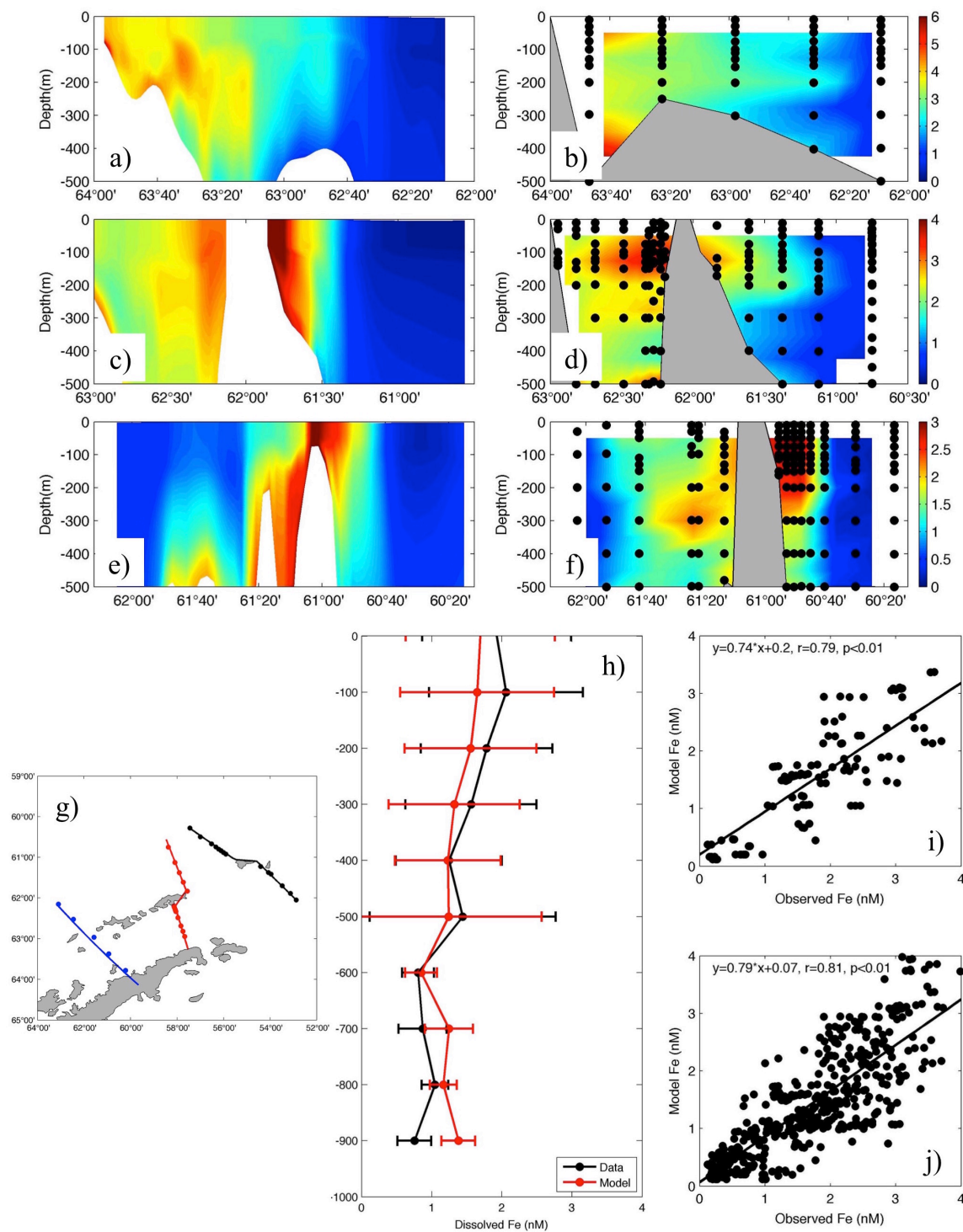
6

Figure 7.



1 Figure 8.

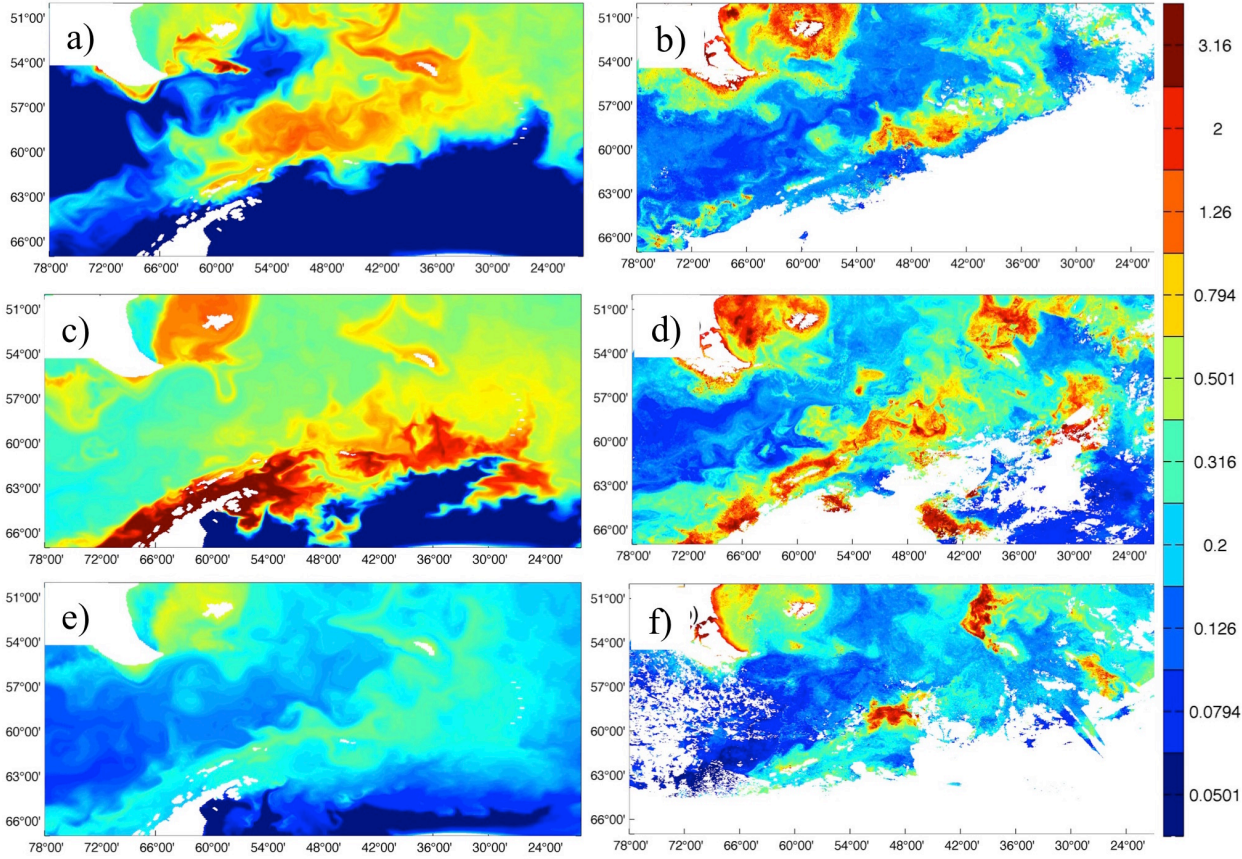
2



3

4

Figure 9.



1 Figure 10.

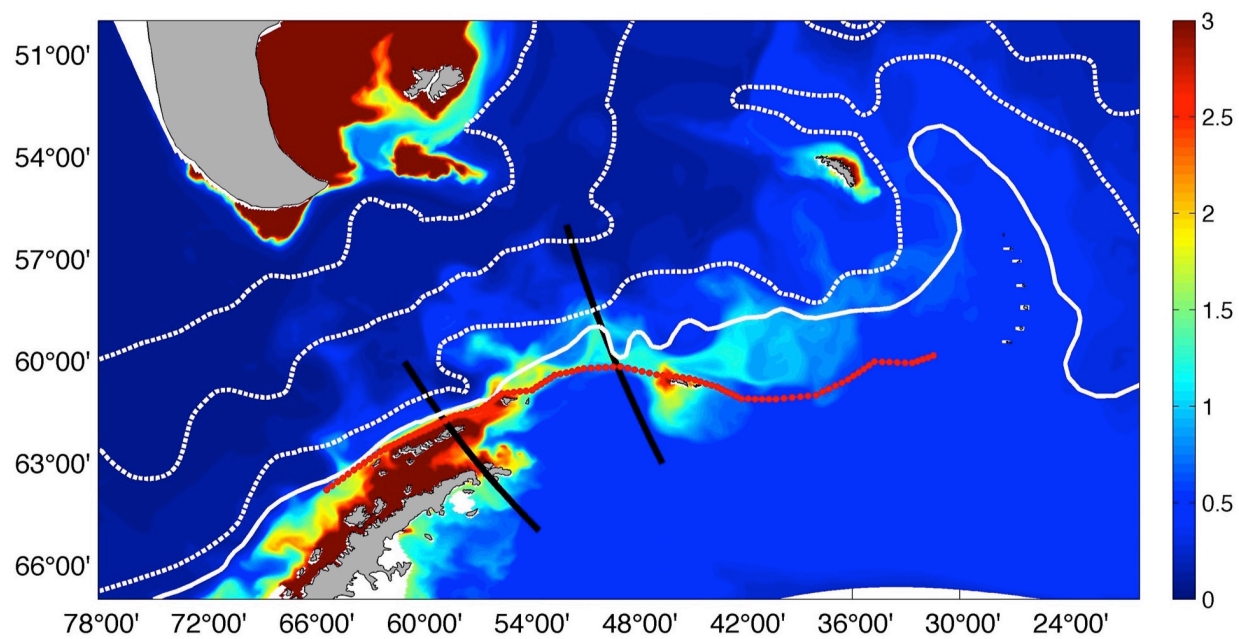
2

3

4

5

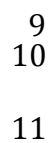
6



7

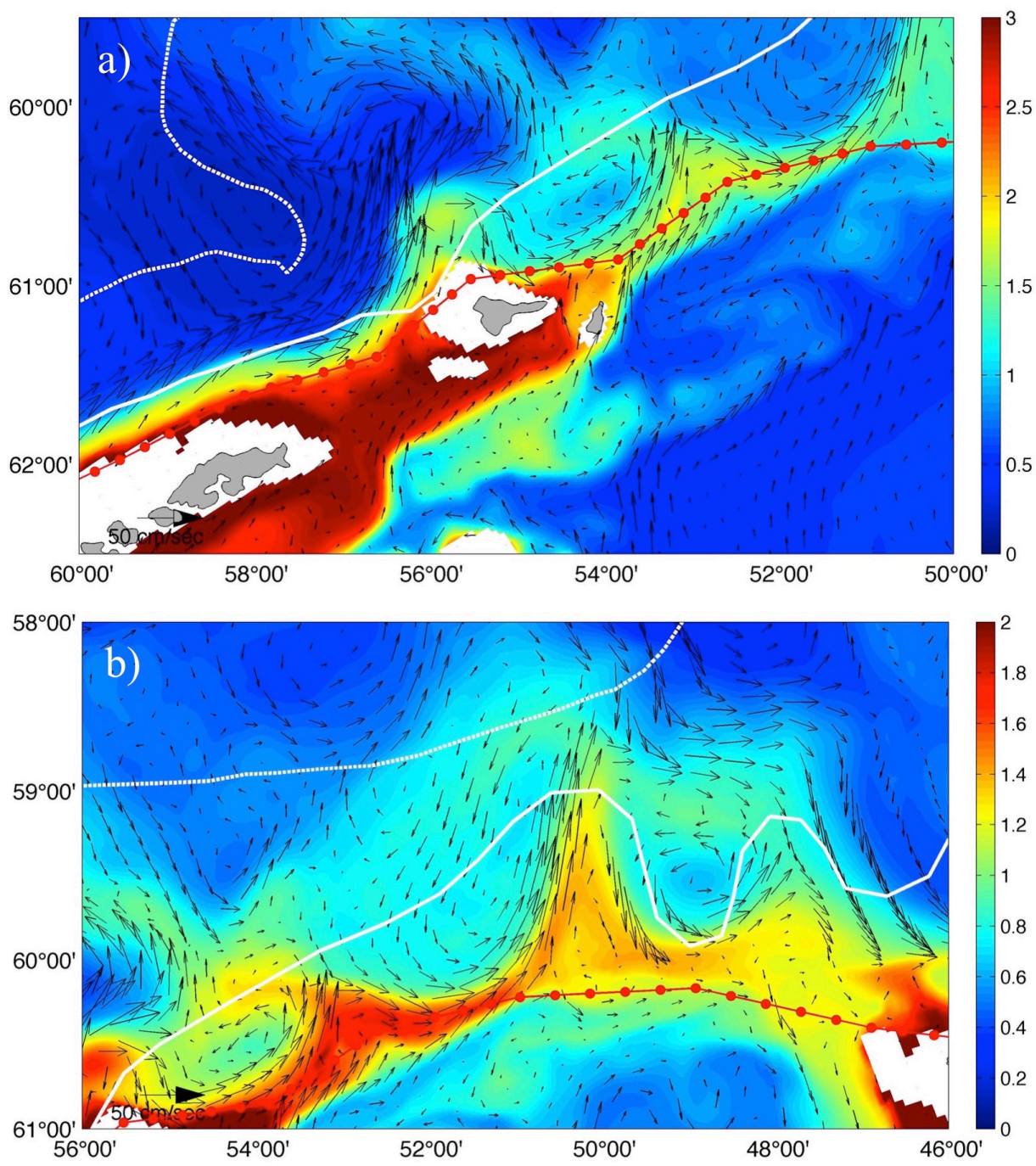
8

- 1
- 2
- 3
- 4
- 5
- 6
- 7
- 8



1 Figure 12.

2

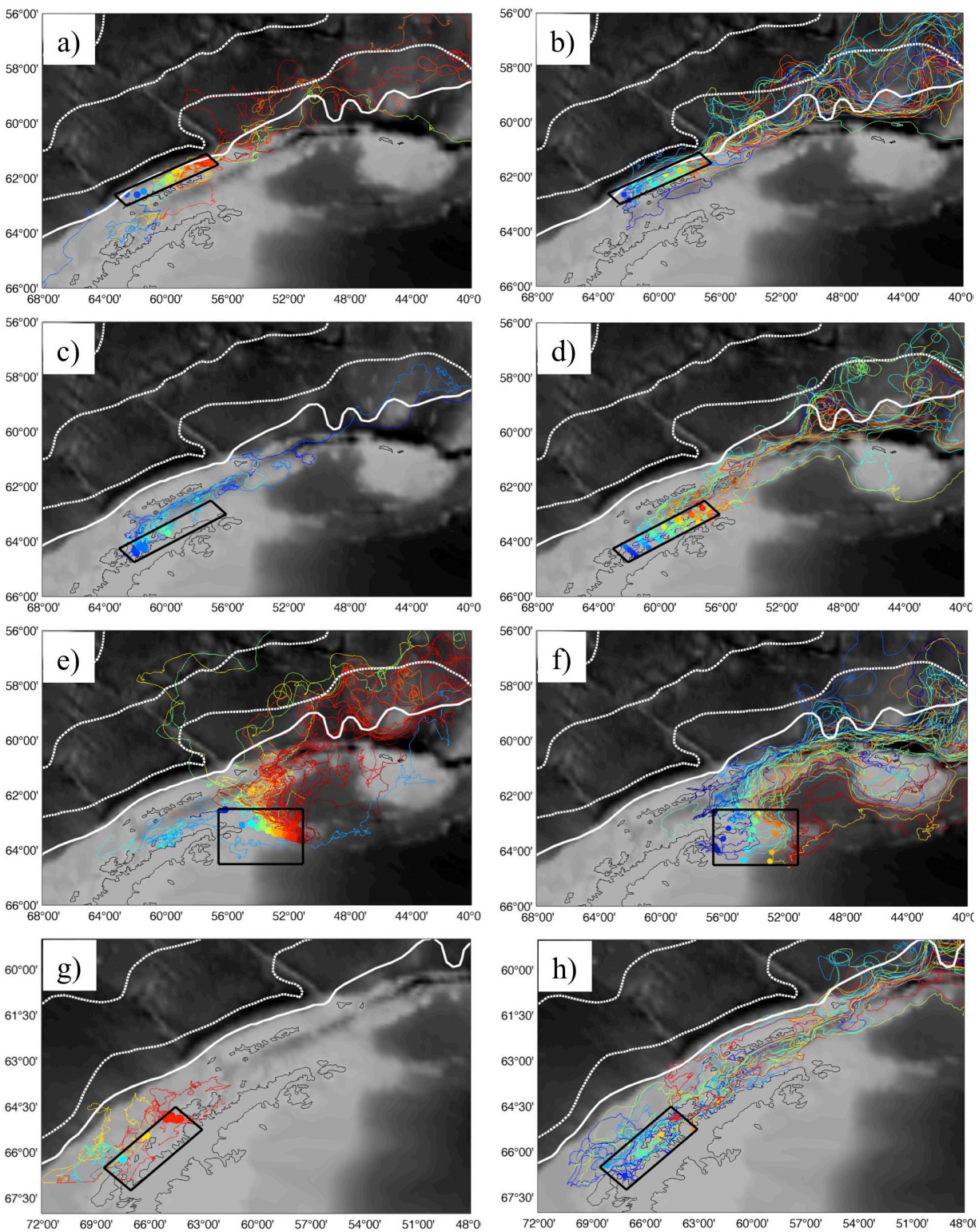


3

4

5

1 Figure 13.
2
3



4

Figure 14.

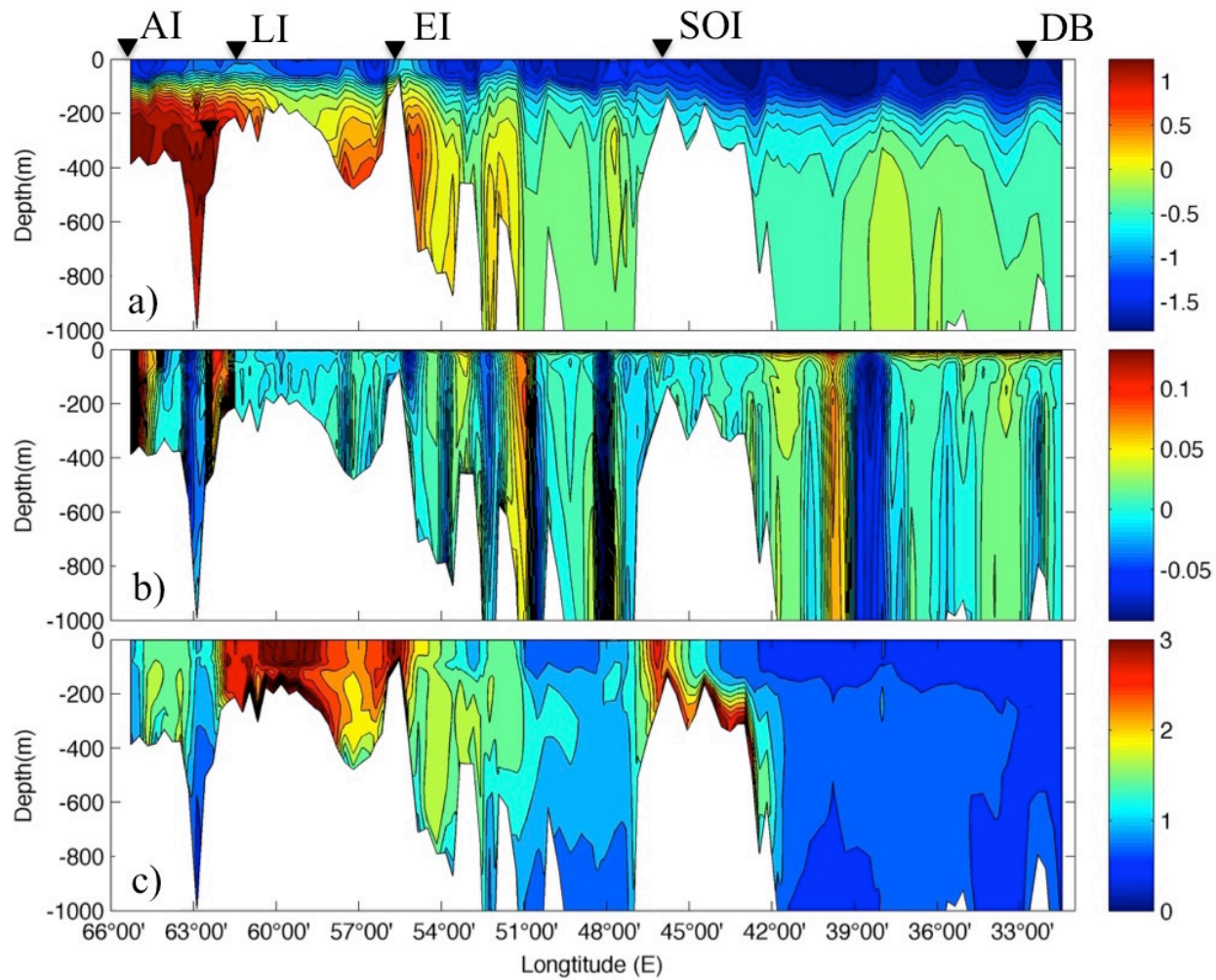


Figure 15.

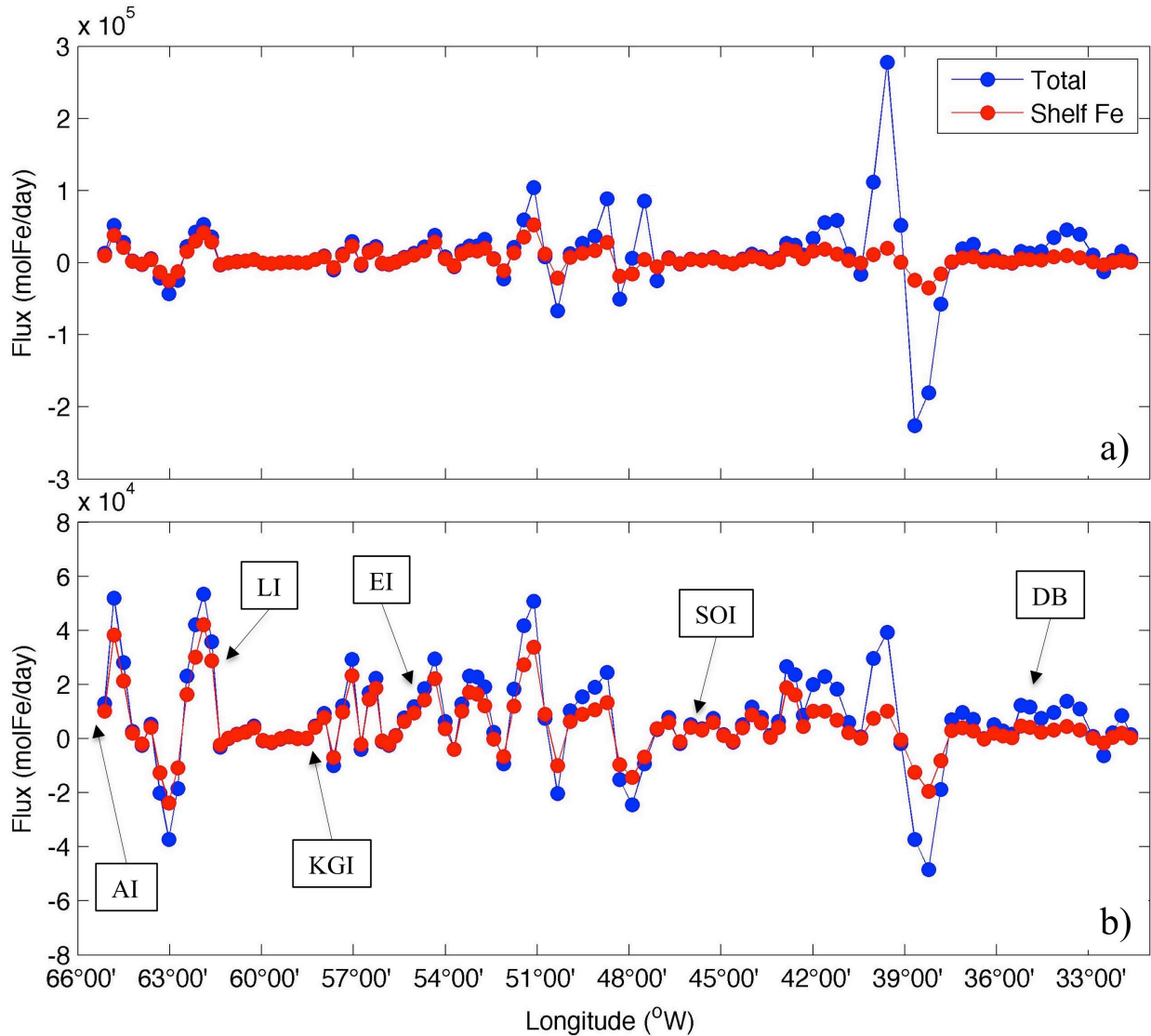


Figure 16.

